Tidal stability of interstellar clouds

By

Blake Lawrence Brian Staples

A thesis submitted to Macquarie University
for the degree of Master of Research
Department of Physics and Astronomy
December 2019

MACQUARIE
University
SYDNEY·AUSTRALIA

Typeset in LaTeX 2_ε.

Except where acknowledged in the customary manner, the material presented in this thesis is, to the best of my knowledge, original and has not been submitted in whole or part for a degree in any university.

Blake Lawrence Brian Staples

Acknowledgements

It is between the lines where entire volumes of failure, frustration, and self-doubt are hidden, cast away in an attempt to present a smooth, intelligible, and coherent thesis. But to ignore these failures is to ignore the true journey, the months spent wondering down the garden path, the sleepless nights and restless days, and the uncertainty in ever obtaining results. This work should stand as a testament to these struggles, not as a monument of the failures, but as a reminder of the real journey, and the strength of willpower.

To say this year went smoothly would not only be dishonest to myself and wilfully ignorant of the physical and mental strain I placed on my body, but also hurtful to my friends and family who I have neglected these past 12 months. There are many names that come to my mind for who I am thankful for helping me to be where I am today, too many to ever be compiled. However, there are several people who I wish to recognise, as I owe them much, as they made sure the success of my thesis was all but guaranteed.

> My supervisor, Mark. Without whom this work would have never been started, let alone completed. When asked for 2 seconds you would give 2 hours without a second thought. You have taught me so much and if I am to succeed in academia it will be because of the foundation you have given me.
>
> My mother, Pam. To whom I will always be indebted to for showing me just how far sheer force of will can carry someone. You have helped shaped me into who I am and without you I would not be anywhere near where I am today.
>
> My partner, Liz. Who always made it so easy to come home and smile, even if it was 3 am, everything was broken, and my hair had turned white and fallen out. I still owe you much for proofreading this thesis far more than I was able to.
>
> My friend, James. Who has always been there to fix my coding woes and show me a better way to do things, be it as a teacher for my first course in programming in undergraduate or the final days of my thesis.

Thank you from the bottom of my heart. This year would not have been possible without all of you.

To my fellow astro kids, Taylah, Lachlan, Sarah, and Caro; who helped me through the most stressful but successful year of my life, who would always entertain my time-wasting questions and try to solve my problems—even if they thought the work was in another language, thank you, you helped make this the best year of my life.

Abstract

The strong gravitational tidal field of supermassive black holes is thought to disrupt nearby interstellar gas clouds, preventing star formation. Recently, bipolar outflows, a "smoking-gun" for recent star formation, have been found within 2 parsecs of Sgr A* - the 4×10^6 $M_\odot$ black hole at the centre of our galaxy.

This work employs a semi-analytic approach based on the tensor virial theorem to describe the gross dynamics of interstellar clouds including tidal fields, external pressure, figure rotation, and internal streaming. A set of coupled ordinary differential equations describing the evolution of the cloud's axes, velocities, and figure are solved for equilibrium states, and their stability is examined by following their evolution in response to a transient perturbation.

Solutions are presented where the physical sizes of the clouds are found as a function of density and axis ratios, which are dependent on the strength of the tidal field. Allowing counter-rotating internal streaming gives rise to two new classes of equilibria, one of which is stable, and for low masses, violates the Roche criterion for tidal disruption.

Contents

List of Figures

1

Introduction

Star formation in the centre of galaxies is thought to be inhibited by the extreme tidal field of supermassive black holes (SMBH)[1]. This made the discovery of an early type star in the Galactic centre, the "Allen-Forrest" star[2,3], surprising. Currently ~ 120 young (<6 Myr) massive (10–100 $M_\odot$) Wolf-Rayet/O-B type stars have been found within ~ 0.5 pc of Sagittarius A* (Sgr A*)[4–6], our galaxy's supermassive black hole. These stars are now thought to have formed due to gravitational instabilities in a disk of rotating material which was captured from a transiting interstellar cloud[7,8]. There is now emerging evidence of ongoing star formation within 2 pc of Sgr A* which is not associated with this process[9–15] and has prompted a renewed investigation into star formation at the Galactic centre. This thesis therefore attempts to address if effects such as the high interstellar pressures, known to be present in the Galactic centre, or rotation can permit tidally stable gas clouds in the presence of supermassive black holes.

1.1 The Galactic centre

The Galactic centre of the Milky Way galaxy lies ~ 8 kpc from Earth[16–20]. This proximity allows for the unique opportunity to observe individual stars and their motions around a $\approx 4 \times 10^6\,M_\odot$ SMBH[6,18,21]. Furthermore, this has allowed for observation of the dynamics of gas clouds in the presence of strong tidal fields[22]. The gas and dust content of the centre of the Milky Way can be broken down into several distinct zones; The central cavity, which extends from the central SMBH out to ~ 1.5 pc, the circumnuclear ring (CNR) which extends from central cavity to ~ 4 pc, and the central molecular zone (CMZ) which extends outwards from ~ 4 pc. This work will focus on the central cavity and CNR—for a further detailed discussion of the conditions in the CNR and CMZ see the recent work by Ferriere[23]; additionally a general review of the Galactic centre is given by Genzel[24].

The central cavity is characterised by an evacuated region devoid of dense gas and dust containing several isolated streams of Hydrogen, usually referred to as Sgr A West or the Mini Spiral[25]. This region is considered devoid of gas as the average gas density is at least one order of magnitude lower than the surrounding CNR[26]. The streams of the Mini Spiral appear as a three armed spiral structure stretching out to the CNR as shown in Figure 1.1 where the streams are differentiated into the Northern Arm, Eastern Arm, Western Arc, and a short Bar. The entire structure has an ionized surface from the intense ultra-violet (UV) radiation emitted from the nearby population of young bright stars. The total mass of the ionized component of the Mini Spiral is $\approx 60\,M_\odot$ with the distribution being $\approx 10, 10, 35$, and $5\,M_\odot$ in the Northern arm, Eastern arm, Western arc, and Bar[25]. The Northern and Eastern arms are infalling material from the CNR and the western arc is likely the ionized inner surface of the CNR[27]. The electron temperature of the ionized components is best fitted by temperatures within the range 5000–11 000 K in the arms and up to 13 000 K in the bar region[28]. While determining the internal composition of these clouds is challenging the most likely outcome is atomic gas[26,29]. The mass of this atomic gas is roughly $\sim 300\,M_\odot$[26], which is associated with the northern and eastern arms of the Mini Spiral—with temperatures of ~ 150 K. Additionally, thermal emission from a few solar masses of dust[30] has been observed with a temperatures of 70–130 K, the presence of this dust implies a few $100\,M_\odot$ of atomic or molecular gas. Little molecular gas has been found in the cavity[31] however, which is to be expected and is readily explained by the intense UV radiation from the young bright stars photo-dissociating the molecules.

The CNR surrounding the central cavity is observed to be a warped, asymmetric, kinematically-unsettled, clumpy torus with a sharp cut-off on the inner-face[22,26,34–36], the ring is argued to be a transient feature of the Galactic centre with an age of $\sim 10^5$ years[36,37]. The composition of the ring is observed to be a mix of molecular and atomic gas (see Ferriere[23] and references within section 2.2). Recent mass estimates for the ring range from 2×10^5–$4\times10^5\,M_\odot$ with associated temperatures of $T \sim 60$ K[35,36]. The density of the ring varies due to the "clumpiness" of the structure, but recent estimates indicate values in the range $\sim 4.5\times10^{4.5}$–$2\times10^6\,\mathrm{cm}^{-3}$[36–38]—significantly lower than earlier estimates which ranged as high as $4\times10^7\,\mathrm{cm}^{-3}$[24]. These densities, when considered in isolation, are too low for star formation to occur without a triggering event[36]. However, 13 water masers—indicative of densities sufficient to overcome the tidal field of Sgr A*—have been observed[32,39].

Early infrared observations of the inner 2 pc of the Milky Way revealed a large number of very bright stars[40–42]. Spectroscopic follow up revealed many of these stars were old (> 1 Gyr), rotated with the galactic rotation, and with an isotropic distribution consistent with accretion of gas or star clusters from the galactic disk[43]. In contrast the population of young stars form 2 (arguably 3) distinct dynamical groups. A group of O and B type stars reside in the "S cluster", a group of stars with highly eccentric orbits about Sgr A* with random orientations with respect to each other[17], while being in a statistically isotropic distribution[44]. The remaining stars are distributed into two distinct rotating disks. These disks rotate in opposite directions in projection, with large ($\sim 115°$) orientation angles from each other, and orbit in opposite directions, although these stars are coeval to within 1 Myr[45]. These different orbital dynamics resulted in several different star formation theories attempting to describe their formation as the tidal shear force from Sgr A* should inhibit star formation in this close vicinity[1,44]. Two main models were proposed to explain this star formation. The *in*

Figure 1.1: Multi-wavelength image of the Galactic centre showing (in red) the 3.4 mm Hydrogen cyanide (HCN) (J = 1 → 0) line emission from the CNR and (in green) the 3.6 cm radio continuum emission from the warm ionised gas in the Mini Spiral. North is up and East is left. Inset: True colour image of ^{13}CO (J = 2 → 1) with velocities between 110–112, 113–114, and 115–117 km/sec in red, green, and blue respectively, showing the CNR and bipolar outflow 1—see Yusef-Zadeh[15]. Main image reproduced from Figure 2 of Ferriere[23] which was created with radio continuum data from Yusef-Zadeh[32] and HCN data from Wright[33]. Figure credit: Farhad Yused-Zadeh. Inset image reproduced from Figure 1 of Yusef-Zadeh[15].

situ formation theory, which proposes a giant molecular cloud came 'close' to Sgr A*, was tidally disrupted, captured, and formed a gravitationally unstable disk around Sgr A* which then fragmented and formed the observed stars[46]. The second theory, the *infall* theory, proposes a massive cluster of stars forms outside the CNR and spirals into the centre through tidal friction with the old stellar population[47]. Both theories fail to completely explain the observed dynamics. For example, in situ formation predicts less eccentric, more coplanar orbits than observed in the two rotating disks;[48] and the infall theory predicts the tidal decay time is significantly longer than the observed ages[45]. Currently the favoured star formation scenario is through the partial accretion of a giant molecular cloud[7].

The mechanism of star formation of the recently observed sources must be significantly different then the scenarios used to explain star formation in the past, this is because the recent observations allure to in situ star formation—not fragmentation of accreting matter. IRS 13N is a cluster of compact sources within ~ 0.15 pc of Sgr A*[9–11,49] that due to their IR excess could be young stellar objects with ages between 0.1–1 Myr. Further out at ≈ 0.6 pc from Sgr A*, located mainly to the North-East of the Mini Spiral 11 clumps of molecular gas indicative of highly embedded protostars have been observed[13]. Further evidence of star formation is provided through observations of the Eastern arm where 44 compact sources, which are candidate photoevaporative protoplanteary disks, and hence newly formed low mass stars[14]. Most recently 11 bipolar outflows within 1 pc of Sgr A* have been found[15]. These outflows are characteristic of young star formation[50,51] and thus provide compelling evidence for in situ star formation in the Galactic centre within the extreme tidal force of Sgr A*.

This evidence for star formation presents a conundrum however, The canonical Roche density, the minimum density a cloud requires to be stable via self-gravity in the presence of an external tidal field, requires cloud densities on the order of $n \sim 1 \times 10^8 \left(\frac{r}{\mathrm{pc}}\right)^{-3}$ to be stable with respect to the tidal field of Sgr A*—this readily surpasses typical densities found in molecular clouds, $n \lessapprox 10^6\,\mathrm{cm}^{-3}$. However, interior to ~ 3 pc of the Galactic centre are several components need to be considered to determine the strength of external pressures. Inside the CNR magnetic fields strengths of order 2–3 mG have been observed[52,53] which recently have been shown to trace the Mini Spiral[54]; these fields result in a magnetic pressure of $p_{\mathrm{ext}}/k_{\mathrm{B}} \sim 2 \times 10^9\,\mathrm{K\,cm}^{-3}$ where p_{ext} is the external pressure and k_{B} is the Boltzmann constant. Furthermore, the temperatures (5000–11 000 K) and electron densities ($n_e \sim 1 \times 10^5\,\mathrm{cm}^{-3}$) of the ionized regions of the Mini Spiral also suggest a pressure of $p_{\mathrm{ext}}/k_{\mathrm{B}} \sim 2 \times 10^9\,\mathrm{K\,cm}^{-3}$. While the thermal pressure in the inner regions of the CNR is slightly less, $p_{\mathrm{ext}}/k_{\mathrm{B}} \sim 3 \times 10^8\,\mathrm{K\,cm}^{-3}$ there is a significant contribution from the turbulent velocity dispersion in the CNR which can yields pressures up to $p_{\mathrm{ext}}/k_{\mathrm{B}} \sim 4 \times 10^{10}\,\mathrm{K\,cm}^{-3}$[55]. These increased pressures, $\sim 10^2$–10^3 interstellar medium values at the galactic disk, could act to compress the clouds aiding stability and thus must be accounted for in the analysis.

1.2 Approach

There is clearly tension between the standard expectations based on the Roche limit and observations of what appear to be isolated young stellar objects (YSO) in the Galactic centre. The canonical formulation of the Roche limit considers a satellite in which its own gravitational force dominates its stability and is tidally locked to the object it orbits. Thus, the Roche limit fails to capture two key characteristics of gas clouds at the Galactic centre. Firstly, external pressures, which are known to be present in the Galactic centre; secondly, tidally locking gas-clouds is difficult due to their low viscosity. Thus, any proper treatment of tidal stability of gas clouds at the Galactic centre requires a proper treatment of external pressures and rotation. The aim of this thesis therefore, is to explore these effects using a robust model with a simple formulation for the combined treatment of external pressures and rotational effects on the stability of gas cloud in the Galactic centre subject to tidal fields from Sgr A*.

To consider the effect of external pressures on gas clouds this thesis will use Bonnor-Ebert Spheres[56,57], self-gravitating isothermal gas clouds with internal and external pressure forces which are in equilibrium. To consider the effect of rotation on the dynamics of the clouds they will be treated as Roche ellipsoids. The Roche ellipsoids describe a homogenous, self-gravitating, and rotating ellipsoid orbiting another body—whose presence is the origin of a tidal force on the ellipsoid. These approximations are sufficiently realistic for gas clouds in the galactic centre; while gas cloud cores are generally centrally clumped the difference in the gravitational force is of order $5/3$. Hence, this thesis aims to create a robust semi-analytic model with a simple formulation for the combined treatment of Bonnor-Ebert Spheres and Roche ellipsoids to assert their stability in the presence of tides and external pressures, the tensor virial theorem provides a direct procedure for this.

The virial theorem (see, e.g. Chandrasekhar[58]) is a way of solving the complex integro-differential equations of physics for an *exact* solution. The virial theorem describes the dynamics of systems through analysis of its moments, and is an exact relation between them. Applying the virial theorem technique to the Euler equations[59], the idealised equations of fluid mechanics, representing the conservation laws of mass, momentum, and energy, results in quantities representing the density distribution of the system. Adopting a non-exact model, e.g. homogenous ellipsoid, allows the resulting integrals to be analytically evaluated. Integrating over the volume of the cloud results in the limitation that only monolithic evolution of the cloud can be followed; there is no description for the evolution of substructure, however this work interested in the global dynamics—if a cloud is tidally disrupted by a black hole variations in substructure, such as fragmentation, are not of key importance. By considering the temporal evolution of the density distribution, the gross dynamics of the system can be obtained.

The virial theorem technique has been used since the early 20th century[60,61] with significant work applying the techniques to hydrodynamical problems, specifically, the formation of stars[62–65]. This has allowed authors to numerically solve the steady state conditions of ellipsoids under the gravitational influence of another body[66]. Recently, authors such as Chen[55] have used the virial theorem approach with the inclusion of external pressures and tidal fields in their calculations of cloud mass and densities for the Galactic centre; specifically finding external pressures which could compress spherical cloud cores in the CNR to densities capable of providing tidal stability.

This thesis will therefore will build on the previous literature to model the evolution of non-spherical pressurised clouds with internal rotation. The equilibrium Roche ellipsoids will be used as the starting point for analysis of Bonnor-Ebert Spheres. The analysis will then be extended to model the additional effects of external tidal fields, and internal rotation to characterise the temporal evolution of gas clouds at the Galactic centre.

1.3 Project outline

This project details the derivation, results, and physical insights from a semi-analytical model describing the evolution of a homogenous, compressible, constant spatial density, isothermal tri-axial ellipsoidal gas cloud in the pressure of tidal fields and external pressures. This work

adopts a simple model on the clouds structure, it is free to rotate in the orbital plane, and has linear velocity fields consistent with the evolving axis ratios, orientation, and streaming of fluid within. The tensor virial theorem is used to obtain the ordinary differential equations (ODEs) describing the evolution of this cloud from which insights into star formation in the strong gravitational regime are obtained.

Chapter 2 outlines the derivation of the model's ODEs from their formulation based on the tensor virial theorem, their numerical implementation, and tests of their numerical reliability. A comparison of the model's observed behaviour and the literature is presented in the first part of Chapter 3 where steady state solutions and perturbations from are given where the model is found to evolve as expected subject to transient perturbations. The unique physical sizes of the clouds is then found as a function of their density and axis ratios which are dependent on the tidal strength. The latter part of the chapters presents an investigation into the competing effects of tides, external pressures, and internal rotation and their effect on the stability where two new equilibria classes for clouds with counter-rotating internal fluid is found. In low mass clouds, one of these solutions is found to be stable, despite being unstable according to the Roche criterion. Following this, in Chapter 4 I conclude with the findings of this research, which is applied to the stability of clouds in the Galactic centre, before mentioning the future prospects.

2

Semi-Analytic Model

This chapter details the derivation and numerical implementation of a semi-analytic model based on the tensor virial theorem to characterise the evolution of gas clouds applicable to the Galactic centre. The evolution of a compressible isothermal fluid under the influence of gravity, pressure, and an external gravitational potential in a rotating reference frame is specified by the equations:

$$\rho \frac{\partial \mathbf{v}}{\partial t} + \rho(\mathbf{v} \cdot \nabla)\mathbf{v} = -\nabla p - \rho \nabla \phi - \rho\, \boldsymbol{\Omega} \times (\boldsymbol{\Omega} \times \mathbf{r}) - 2\rho\, \boldsymbol{\Omega} \times \mathbf{v}, \tag{2.1}$$

$$\frac{\partial \rho}{\partial t} + \nabla \cdot (\rho \mathbf{v}) = 0, \tag{2.2}$$

$$p(\rho) = \rho c_s^2, \tag{2.3}$$

where ρ is the density, $\mathbf{v}$ is the velocity of the fluid, p is the pressure, ϕ is the gravitational potential; $\mathbf{r}$ is the distance from the origin of the rotating frame to the point of interest and $\boldsymbol{\Omega}$ is the angular velocity of the point $\mathbf{r}$ about the origin; boldface represents a three-dimensional vector, and c_s is the isothermal sound speed.

These equations are used to create a model of a compressible isothermal tri-axial ellipsoidal gas cloud with constant spatial density orbiting a black hole. The external pressure, p_{ext}, is accounted for by asserting that $p = p_{\text{ext}}$ at the cloud surface. The gravitational potential is be split into contributions from the cloud and the black hole. The figure of the cloud is allowed to rotate in the orbital plane, additionally, the internal fluid is allowed to stream relative to the figure rotation. The mass of the cloud is constant because the boundary moves with the fluid.

Multiplying Equation 2.1 by the spatial component $x_j,\ j = 1, 2, 3$ and integrating it over the instantaneous volume, $V(t)$, occupied by the cloud yields the 2nd order *tensor virial*

theorem equation in a rotating reference frame,

$$\dot{\mathcal{H}}_{ij} = 2K_{ij} + \Pi_{ij} + W_{ij} + \mathcal{W}_{ij} + C_{ij}, \tag{2.4}$$

where the subscript ij represents the index in a 3×3 tensor [cf. The work by Chandrasekhar[58,66]]. $\dot{\mathcal{H}}$ represents the inertial term, K the bulk kinetic energy, Π the pressure, W the self-gravitational potential energy, $\mathcal{W}$ the net tidal force from the black hole and centrifugal force, and C is the Coriolis force. Previous works have considered systems in which diagonal symmetry of the tensors is imposed, in this case $\dot{\mathcal{H}}$ becomes the canonical variable $\ddot{I}$, representing the second derivative of the moment of inertia—the model presented in this work does not symmetrise the tensors—allowing for asymmetries in the forces and velocities. For a reference frame rotating about the $i = 3$ axis the tensor terms are explicitly given by:

$$\dot{\mathcal{H}}_{ij} = \frac{d}{dt}\int_V \rho v_i x_j \, dV, \tag{2.5}$$

$$K_{ij} = \frac{1}{2}\int_V \rho v_i v_j \, dV, \tag{2.6}$$

$$\Pi_{ij} = -\int_V x_j \frac{\partial}{\partial x_i} p \, dV, \tag{2.7}$$

$$W_{ij} = \int_V \rho x_j \frac{\partial}{\partial x_i}\phi_{\rm BH} \, dV, \tag{2.8}$$

$$\mathcal{W}_{ij} = -\int_V \rho x_j \left(\frac{\partial}{\partial x_i}\phi_{\rm ext} - \epsilon_{ik3}\epsilon_{lk3}\Omega^2 x_l\right) dV, \tag{2.9}$$

$$C_{ij} = 2\Omega \int_V \epsilon_{il3}\rho v_l x_j \, dV, \tag{2.10}$$

where ϵ_{ijk} is the Levi-Civita symbol and Einstein summation notation is implied on the repeated indices, k and l. The integrals are calculated over the volume of the cloud which is not fixed in space. A schematic of the system is shown in Figure 2.1, where a tri-axial ellipsoid rotates in the $\hat{x}_1$, $\hat{x}_2$ plane at a distance $r_0\hat{x}_1$ from a central potential (black hole) where the reference frame rotates at the Keplerian orbital velocity of the cloud [$\Omega_0^2 = \frac{Gm_{\rm bh}}{|\mathbf{r_0}|^3}$, where $m_{\rm bh}$ is the mass of the black hole and G is the gravitational constant].

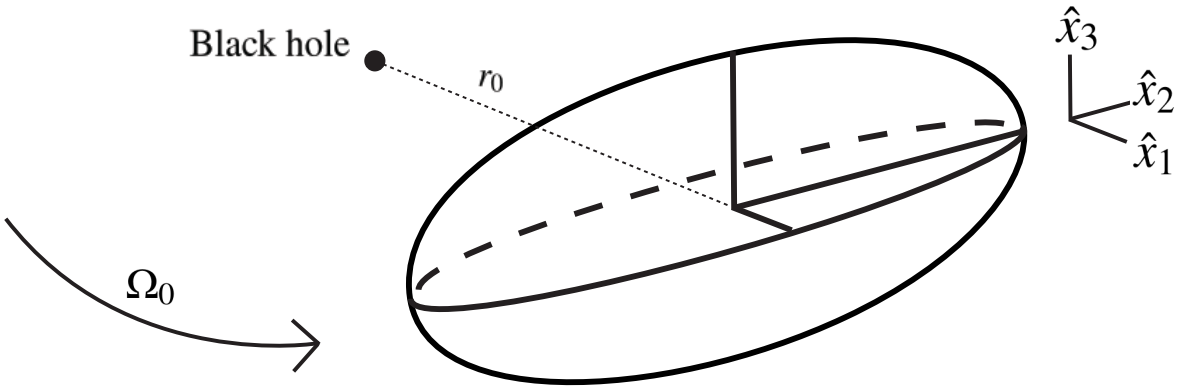

Figure 2.1: Geometric configuration for a tri-axial ellipsoid in a spherical orbit in the $\hat{x}_1, \hat{x}_2$ plane centred at a distance $r_0\hat{x}_1$ from a black hole with angular rotation Ω_0 about the $\hat{x}_3$ axis. The ellipsoid is allowed to rotate around its centre about the $\hat{x}_3$ direction.

The integrals over the cloud volume (Equations 2.5 – 2.10) at each instant in time are most straightforwardly calculated in a static reference frame where the principal axes of the cloud are along the canonical unit vectors of a Cartesian coordinate system. To change from the *orbital frame* with variables $x_1,\ x_2,\ x_3$ into the *cloud frame* with variables $\xi_1,\ \xi_2,\ \xi_3$, that is, from the rotating reference frame centred on the black hole [where Equations 2.5 – 2.10 are formulated], into a frame characterising an ellipsoid with major axes along the unit vector directions, a rotation by an angle $\theta(t)$ is required. In the cloud frame each point $\boldsymbol{\xi}_1,\ \boldsymbol{\xi}_2,\ \boldsymbol{\xi}_3$ can be transformed into the orbital frame through the linear mapping

$$\begin{pmatrix} x_1 \\ x_2 \\ x_3 \end{pmatrix} = \begin{pmatrix} \cos(\theta) & -\sin(\theta) & 0 \\ \sin(\theta) & \cos(\theta) & 0 \\ 0 & 0 & 1 \end{pmatrix} \begin{pmatrix} \xi_1 \\ \xi_2 \\ \xi_3 \end{pmatrix}. \tag{2.11}$$

This allows for analytic solutions to the integrals to be readily calculated and expressed in the orbital frame. A schematic of this rotation is shown in Figure 2.2 where the major axes of the ellipsoid (black) are now rotated by an angle θ with respect to the static coordinate system of the black hole (green) where the vector from the black hole to the centre of the ellipsoid is purely in the $\hat{x}_1$ direction.

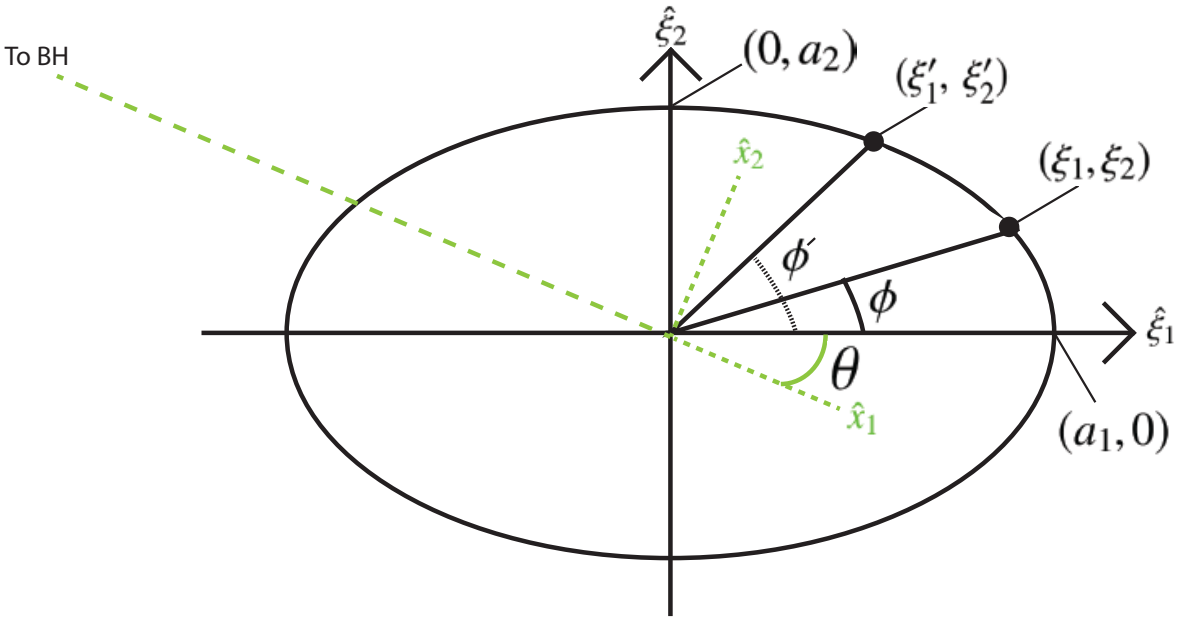

Figure 2.2: Top-down diagram showing the mapping of the orbital frame unit vectors (green) to the cloud frame unit vectors (black) through a rotation by an angle $\theta(t)$. Additionally shown is a fluid particle at time t located at position $(\xi_1,\ \xi_2)$ which is allowed to rotate to a position $(\xi_1',\ \xi_2')$ at time t' with respect to the figure.

2.1 Velocity field

The model adopts a linear velocity field in the cloud, constrained to be consistent with the evolution of the cloud's figure, but allowing for internal fluid streaming with respect to the figure of the ellipsoid, restricted to be parallel to the plane of orbit. In the orbital plane the components of the ξ_1 and ξ_2 axes are coupled, while the ξ_3 velocity in the perpendicular plane is decoupled. This coupling of the ξ_1 and ξ_2 axes allows the fluid to rotate at a rate, $\dot{\phi}$, with respect to its initial position on the figure—allowing it to drift. However, it is required that the fluid particles maintain their position with respect to each other—i.e. a fluid particle initially on the boundary must always be the boundary. A schematic showing a fluid particle at location $(\xi_1,\ \xi_2)$ at time t moving to location $(\xi_1',\ \xi_2)$ at time t' is shown in Figure 2.2.

The velocities of the fluid inside the cloud are therefore given by

$$\frac{d}{dt}\xi_1 = \alpha\xi_1 + \beta\xi_2, \tag{2.12}$$

$$\frac{d}{dt}\xi_2 = \gamma\xi_1 + \delta\xi_2, \tag{2.13}$$

$$\frac{d}{dt}\xi_3 = \lambda\xi_3, \tag{2.14}$$

where $\alpha,\ \beta,\ \gamma,\ \delta$, and λ are constants to be found such that the ellipsoid does not deform from its characteristic shape. Differentiating the equation for a tri-axial ellipsoid with respect to position, substituting these constants in, yields the relationships

$$\alpha = \frac{\dot{a}_1}{a_1}, \tag{2.15}$$

$$\delta = \frac{\dot{a}_2}{a_2}, \tag{2.16}$$

$$\frac{\beta}{a_1^2} = -\frac{\gamma}{a_2^2}, \tag{2.17}$$

$$\lambda = \frac{\dot{a}_3}{a_3}, \tag{2.18}$$

where a_i is the length of the axis in the i direction and $\dot{a}_i$ its temporal derivative. This thesis adopts the symbol $\dot{\phi} \equiv \gamma$ as it corresponds to the angular velocity of the fluid with respect to the a_1 axis. This definition along with Equation 2.13 allows the velocity relationship (Equation 2.17) to be obtained as

$$\gamma = \dot{\phi} \implies \beta = -\frac{a_1^2}{a_2^2}\dot{\phi}. \tag{2.19}$$

Thus, the three velocity equations in the cloud frame are given by:

$$\dot{\xi}_1 = \frac{\dot{a}_1}{a_1}\xi_1 - \frac{a_1}{a_2}\dot{\phi}\xi_2, \tag{2.20}$$

$$\dot{\xi}_2 = \frac{a_2}{a_1}\dot{\phi}\xi_1 + \frac{\dot{a}_2}{a_2}\xi_2, \tag{2.21}$$

$$\dot{\xi}_3 = \frac{\dot{a}_3}{a_3}\xi_3. \tag{2.22}$$

In the orbital frame the velocity field inside the gas cloud is

$$\frac{d}{dt}x_1 = \frac{d}{dt}(\xi_1\cos(\theta) - \xi_2\sin(\theta)) = \dot{\xi}_1\cos(\theta) - \xi_1\dot{\theta}\sin(\theta) - \dot{\xi}_2\sin(\theta) - \xi_2\dot{\theta}\cos(\theta), \quad (2.23)$$

$$\frac{d}{dt}x_2 = \frac{d}{dt}(\xi_1\sin(\theta) + \xi_2\cos(\theta)) = \dot{\xi}_2\sin(\theta) + \xi_1\dot{\theta}\cos(\theta) + \dot{\xi}_2\cos(\theta) - \xi_2\dot{\theta}\sin(\theta), \quad (2.24)$$

$$\frac{d}{dt}x_3 = \frac{d}{dt}\xi_3 = \dot{\xi}_3, \quad (2.25)$$

where substituting the relations from Equation 2.20–2.22 yields

$$\dot{x}_1 = \xi_1\left[\frac{\dot{a}_1}{a_1}\cos(\theta) - \left(\frac{a_2}{a_1}\dot{\phi} + \dot{\theta}\right)\sin(\theta)\right] + \xi_2\left[-\frac{\dot{a}_2}{a_2}\sin(\theta) - \left(\frac{a_1}{a_2}\dot{\phi} + \dot{\theta}\right)\cos(\theta)\right], \quad (2.26)$$

$$\dot{x}_2 = \xi_1\left[\frac{\dot{a}_1}{a_1}\sin(\theta) + \left(\frac{a_2}{a_1}\dot{\phi} + \dot{\theta}\right)\cos(\theta)\right] + \xi_2\left[\frac{\dot{a}_2}{a_2}\cos(\theta) - \left(\frac{a_1}{a_2}\dot{\phi} + \dot{\theta}\right)\sin(\theta)\right], \quad (2.27)$$

$$\dot{x}_3 = \xi_3\left[\frac{\dot{a}_3}{a_3}\right]. \quad (2.28)$$

These correspond to the v_i terms appearing in the virial theorem integrals.

2.2 Evaluation of the tensors

In the orbital frame the linearity of the component moments, fluid velocities, and gravitational potentials results in the evolution of the cloud being characterised by integrals of the form

$$\int_V x_i x_j \, dV. \quad (2.29)$$

The linearity of the coordinate transformation between the orbital frame and the cloud frame allows these to be expressed in the cloud frame as combinations of

$$\int_V \xi_i\xi_j \, dV = \begin{cases} \frac{4}{15}\pi a_1 a_2 a_3 a_i^2 & i = j, \\ 0 & i \neq j. \end{cases} \quad (2.30)$$

This description allows for the straightforward evaluation of integrals with analytic solutions. For example, consider the object x_1x_1, the integral over the volume of the cloud is given by

$$\int_V \rho x_1 x_1 \, dV = \rho\int_V \xi_1^2\cos^2(\theta) + \xi_2^2\sin^2(\theta) - \xi_1\xi_2\sin(2\theta) \, dV, \quad (2.31)$$

where the condition of constant spatial density was used to bring ρ outside the integral sign. By symmetry any term $\xi_i\xi_j, \;\; i \neq j$ under the integral sign will vanish. This is because any plane of symmetry of mass is a plane of symmetry of the product of inertia $\left(\int_V \xi_i\xi_j \, dV, i \neq j\right)$, and in the ellipsoids own reference frame [cloud frame] every plane is a plane of symmetry of mass and will be strictly zero. Thus, the quantity evaluates to

$$\rho\int_V \left(\xi_1^2\cos^2(\theta) + \xi_2^2\sin^2(\theta)\right) dV = \frac{1}{5}m\left(a_1^2\cos^2(\theta) + a_2^2\sin^2(\theta)\right), \quad (2.32)$$

where m is the mass of the cloud.

2.2.1 Inertial term, $\dot{\mathcal{H}}_{ij}$

The left-hand-side of the tensor virial theorem (Equation 2.4) is

$$\dot{\mathcal{H}}_{ij} = \frac{d}{dt}\int_V \rho v_i x_j \, dV. \tag{2.33}$$

Substituting the relations from Equations 2.11 and 2.26–2.28 for x_j and v_i and integrating in the manner described in Section 2.2 results in five non-zero components of $\dot{\mathcal{H}}_{ij}$. Taking the temporal derivative of these equations yields,

$$\begin{aligned}\dot{\mathcal{H}}_{11} = \frac{m}{5}\Bigg[&\ddot{a}_1 a_1 \cos^2(\theta) + \ddot{a}_2 a_2 \sin^2(\theta) - \frac{1}{2}\ddot{\theta}\left(a_1^2 - a_2^2\right)\sin(2\theta) \\ &+ \dot{a}_1\left(\dot{a}_1\cos^2(\theta) - 2a_1\dot{\theta}\sin(2\theta)\right) + \dot{a}_2\left(\dot{a}_2\sin^2(\theta) + 2a_2\dot{\theta}\sin(2\theta)\right) \\ &- \dot{\theta}^2\left(a_1^2 - a_2^2\right)\cos(2\theta)\Bigg],\end{aligned} \tag{2.34}$$

$$\begin{aligned}\dot{\mathcal{H}}_{22} = \frac{m}{5}\Bigg[&\ddot{a}_1 a_1 \sin^2(\theta) + \ddot{a}_2 a_2 \cos^2(\theta) + \frac{1}{2}\ddot{\theta}\left(a_1^2 - a_2^2\right)\sin(2\theta) \\ &+ \dot{a}_1\left(\dot{a}_1\sin^2(\theta) + 2a_1\dot{\theta}\sin(2\theta)\right) + \dot{a}_2\left(\dot{a}_2\cos^2(\theta) - 2a_2\dot{\theta}\sin(2\theta)\right) \\ &+ \dot{\theta}^2\left(a_1^2 - a_2^2\right)\cos(2\theta)\Bigg],\end{aligned} \tag{2.35}$$

$$\dot{\mathcal{H}}_{33} = \frac{m}{5}\left[\ddot{a}_3 a_2 + \dot{a}_3^2\right], \tag{2.36}$$

$$\begin{aligned}\dot{\mathcal{H}}_{12} = \frac{m}{5}\Bigg[&\frac{1}{2}(\ddot{a}_1 a_1 - \ddot{a}_2 a_2)\sin(2\theta) - \ddot{\theta}\left(a_1^2\sin^2(\theta) + a_2^2\cos^2(\theta)\right) - \ddot{\phi}a_1 a_2 \\ &+ \frac{1}{2}\left(\dot{a}_1^2 - \dot{a}_2^2\right)\sin(2\theta) - \dot{\theta}^2\left(a_1^2 - a_2^2\right)\sin(2\theta) - \dot{\phi}(\dot{a}_1 a_2 + \dot{a}_2 a_1) \\ &+ \dot{\theta}\left(\dot{a}_1 a_1\left(\cos^2(\theta) - 3\sin^2(\theta)\right) + \dot{a}_2 a_2\left(\sin^2(\theta) - 3\cos^2(\theta)\right)\right)\Bigg],\end{aligned} \tag{2.37}$$

$$\begin{aligned}\dot{\mathcal{H}}_{21} = \frac{m}{5}\Bigg[&\frac{1}{2}(\ddot{a}_1 a_1 - \ddot{a}_2 a_2)\sin(2\theta) + \ddot{\theta}\left(a_1^2\cos^2(\theta) + a_2^2\sin^2(\theta)\right) + \ddot{\phi}a_1 a_2 \\ &+ \frac{1}{2}\left(\dot{a}_1^2 - \dot{a}_2^2\right)\sin(2\theta) - \dot{\theta}^2\left(a_1^2 - a_2^2\right)\sin(2\theta) + \dot{\phi}(\dot{a}_1 a_2 + \dot{a}_2 a_1) \\ &- \dot{\theta}\left(\dot{a}_1 a_1\left(\sin^2(\theta) - 3\cos^2(\theta)\right) + \dot{a}_2 a_2\left(\cos^2(\theta) - 3\sin^2(\theta)\right)\right)\Bigg].\end{aligned} \tag{2.38}$$

A further detailed derivation of the inertial term is given in Appendix A.

2.2.2 Kinetic energy, K_{ij}

The kinetic energy tensor components are

$$K_{ij} = \frac{1}{2}\int_V \rho v_i v_j \, dV. \tag{2.39}$$

Evaluating the tensor terms in the prescribed manner of Section 2.2 where v_i and v_j are given by Equations 2.26 – 2.28 yields five non-zero kinetic energy tensor components,

$$\begin{aligned} K_{11} = \frac{m}{10}\Bigg[& \dot{a}_1\left(\dot{a}_1\cos^2(\theta) - a_1\sin(2\theta)\left(\frac{a_2}{a_1}\dot{\phi} + \dot{\theta}\right)\right) \\ & + \dot{a}_2\left(\dot{a}_2\sin^2(\theta) + a_2\sin(2\theta)\left(\frac{a_1}{a_2}\dot{\phi} + \dot{\theta}\right)\right) \\ & + \dot{\theta}^2\left(a_1^2\sin^2(\theta) + a_2^2\cos^2(\theta)\right) \\ & + \dot{\phi}^2\left(a_1^2\cos^2(\theta) + a_2^2\sin^2(\theta)\right) + 2a_1a_2\dot{\theta}\dot{\phi}\Bigg], \end{aligned} \tag{2.40}$$

$$\begin{aligned} K_{22} = \frac{m}{10}\Bigg[& \dot{a}_1\left(\dot{a}_1\sin^2(\theta) + a_1\sin(2\theta)\left(\frac{a_2}{a_1}\dot{\phi} + \dot{\theta}\right)\right) \\ & + \dot{a}_2\left(\dot{a}_2\cos^2(\theta) - a_2\sin(2\theta)\left(\frac{a_1}{a_2}\dot{\phi} + \dot{\theta}\right)\right) \\ & + \dot{\theta}^2\left(a_1^2\cos^2(\theta) + a_2^2\sin^2(\theta)\right) \\ & + \dot{\phi}^2\left(a_1^2\sin^2(\theta) + a_2^2\cos^2(\theta)\right) + 2a_1a_2\dot{\theta}\dot{\phi}\Bigg], \end{aligned} \tag{2.41}$$

$$K_{33} = \frac{m}{10}\left[\dot{a}_3^2\right], \tag{2.42}$$

$$\begin{aligned} K_{12} = K_{21} = \frac{m}{10}\Bigg[& \frac{1}{2}\left(\dot{a}_1^2 - \dot{a}_2^2 + \left(\dot{\phi}^2 - \dot{\theta}^2\right)\left(a_1^2 - a_2^2\right)\right)\sin(2\theta) \\ & + \left(\dot{\theta}(\dot{a}_1a_1 - \dot{a}_2a_2) + \dot{\phi}(\dot{a}_1a_2 - \dot{a}_2a_1)\right)\cos(2\theta)\Bigg]. \end{aligned} \tag{2.43}$$

2.2.3 Pressure tensor, Π_{ij}

The pressure tensor is calculated using

$$\Pi_{ij} = -\int_V x_j \frac{\partial p}{\partial x_i}\, dV, \tag{2.44}$$

where on the surface of the cloud p obtains a value of $p_{\rm ext}$ = constant. Using the product rule in reverse yields

$$\Pi_{ij} = -\int_V \frac{\partial}{\partial x_i}\left(x_j p\right)\, dV + \int_V p \frac{\partial}{\partial x_i} x_j\, dV, \tag{2.45}$$

which by applying the divergence theorem to the first integral and simplifying the second results in

$$\Pi_{ij} = -\oint_S x_j p \cdot ds_i + \delta_{ij} \int_V p\, dV. \tag{2.46}$$

Thus, the net pressure terms are given by

$$\Pi_{11} = \Pi_{22} = \Pi_{33} = (p - p_{\rm ext})V \equiv m c_s^2 - p_{\rm ext} V, \tag{2.47}$$

where $c_s = \sqrt{\frac{k_{\rm B} T}{\mu m_{\rm H}}}$ is the isothermal sound speed, and V is the volume of the ellipsoid.

2.2.4 Self-gravity, W_{ij}

The clouds self-gravitational contribution is calculated by

$$W_{ij} = \int_V x_j \frac{\partial}{\partial x_i} \phi_{\text{self}} \, dV, \tag{2.48}$$

where ϕ_{self} is the self-gravitational potential in the orbital frame. This is expressed in terms of the self-gravity components in the cloud frame, where[65],

$$\frac{\partial}{\partial \xi_i} \phi'_{\text{self}} = -2\rho\pi G a_1 a_2 a_3 A_i \xi_i, \tag{2.49}$$

and A_i are constants related to the geometry of the ellipsoid given by[65]

$$A_i = \int_0^\infty \frac{d\lambda}{\Delta (a_i^2 + \lambda)}, \tag{2.50}$$

and $\Delta^2 = (a_1^2 + \lambda)(a_2^2 + \lambda)(a_3^2 + \lambda)$. These integrals are readily expressible in terms of the degenerate Carlson symmetric form of the third elliptic integral,

$$R_D(x, y, z) = R_J(x, y, z, z) = \frac{3}{2} \int_0^\infty \frac{d\lambda}{(\lambda + z)\sqrt{(\lambda + x)(\lambda + y)(\lambda + z)}}. \tag{2.51}$$

Transforming back to the orbital frame yields five non-zero self-gravitational components:

$$W_{11} = -\frac{3Gm^2}{10} \left[a_1^2 A_1 \cos^2(\theta) + a_2^2 A_2 \sin^2(\theta) \right], \tag{2.52}$$

$$W_{22} = -\frac{3Gm^2}{10} \left[a_1^2 A_1 \sin^2(\theta) + a_2^2 A_2 \cos^2(\theta) \right], \tag{2.53}$$

$$W_{33} = -\frac{3Gm^2}{10} \left[a_3^2 A_3 \right], \tag{2.54}$$

$$W_{12} = W_{21} = -\frac{3Gm^2}{20} \left[\left(a_1^2 A_1 - a_2^2 A_2 \right) \sin(2\theta) \right]. \tag{2.55}$$

2.2.5 Tidal field, $\mathcal{W}_{ij}$

The net contribution from the black hole's gravitational force and the centrifugal force is

$$\mathcal{W}_{ij} = -\int_V \rho x_j \left[\frac{\partial}{\partial x_i}\phi_{\rm BH} - \epsilon_{ik3}\epsilon_{lk3}\Omega^2 x_l\right] dV. \tag{2.56}$$

The distance between the black hole and the gas clouds is orders of magnitude larger than the Schwarzschild radius (~ 0.1 AU), thus the force of the black hole is

$$\frac{\partial}{\partial x_i}\phi_{\rm BH} = \frac{Gm_{\rm BH}}{r^2}\hat{r} \equiv \Omega^2\mathbf{r}, \tag{2.57}$$

where $\mathbf{r}$ is the distance from the black hole to a point inside the cloud. The definition of the angular rotation, Ω, being about the $\hat{x}_3$ axis results in the only non-zero term of $\frac{\partial}{\partial x_i}\Omega$ being $\frac{\partial}{\partial x_1}\Omega$. As $r_0 \gg \xi_i\ \forall i$ a linear Taylor series approximation is used to compute the effect of tides from the black hole. Performing an expansion for $(r_0 + \boldsymbol{\xi} \equiv (r_0 + \xi_1,\ \xi_2,\ \xi_3))$ about the centre of the cloud yields,

$$\begin{aligned}\mathbf{r}\Omega^2 \approx \Big[r_0 + \xi_1,\ \xi_2,\ \xi_3\Big]\Big[&\Omega^2(r_0+\boldsymbol{\xi}) + \frac{\partial}{\partial x_1}\Omega^2(r_0+\boldsymbol{\xi}) \times [r_0 + \xi_1 - r_0],\\ &\Omega^2(r_0+\boldsymbol{\xi}),\ \Omega^2(r_0+\boldsymbol{\xi})\Big],\end{aligned} \tag{2.58}$$

where 2nd order and higher terms have been neglected. The value of Ω is approximated by

$$\Omega^2(r_0+\boldsymbol{\xi}) = \Omega^2(r_0+\xi_1) \overset{\text{def}}{=} \frac{Gm_{\rm BH}}{[r_0+\xi_1]^3} \approx \frac{Gm_{\rm BH}}{r_0^3} \overset{\text{def}}{=} \Omega_0^2. \tag{2.59}$$

Thus,

$$\mathbf{r}\Omega^2 \approx [r_0 + \xi_1,\ \xi_2,\ \xi_3]\left[\Omega_0^2 + \frac{\partial}{\partial x_1}\Omega^2(r_0+\xi_1)[\xi_1\hat{x}_1],\ \Omega_0^2,\ \Omega_0^2\right]. \tag{2.60}$$

The derivative term,

$$\frac{\partial}{\partial x_1}\Omega^2 = \frac{\partial}{\partial x_1}\frac{m_{\rm BH}}{|r_0+\xi_1|^3}, \tag{2.61}$$

yields

$$\frac{\partial}{\partial x_1}\Omega^2\Big|_{r_0+\xi_1} = -\frac{3\Omega_0^2}{|r_0|}\hat{x}_1. \tag{2.62}$$

Thus, the gravitational acceleration from the black hole is given by

$$\frac{\partial}{\partial x_i}\phi_{\rm BH} = \mathbf{r}\Omega^2 \approx [r_0 + \xi_1,\ \xi_2,\ \xi_3]\left[\Omega_0^2 - \frac{3\xi_1\Omega_0^2}{r_0},\ \Omega_0^2,\ \Omega_0^2\right], \tag{2.63}$$

which by neglecting second order terms yields

$$\frac{\partial}{\partial x_i}\phi_{\rm BH} = \Omega_0^2[r_0 - 2\xi_1,\ \xi_2,\ \xi_3]. \tag{2.64}$$

The centrifugal force is calculated in a similar way also using a first order Taylor series

approximation. The contribution is calculated by

$$\epsilon_{ik3}\epsilon_{lk3}\Omega^2 \approx \Omega_0^2\Big[\delta_{1l}[r_0+\xi_l]\hat{x}+\delta_{2l}\xi_l\hat{y}\Big] = \Omega_0^2[r_0+\xi_1,\ \xi_2,\ 0]. \tag{2.65}$$

Thus the net gravitational force by the black hole and the centrifugal force is approximated by

$$\frac{\partial}{\partial x_i}\phi_{\mathrm{BH}} - \epsilon_{ik3}\epsilon_{lk3}\Omega^2 \approx \Omega_0^2[r_0-2\xi_1,\ \xi_2,\ \xi_3] - \Omega_0^2[r_0+\xi_1,\ \xi_2,\ 0], \tag{2.66}$$

$$= \Omega_0^2[-3\xi_1,\ 0,\ \xi_3]. \tag{2.67}$$

Thus, the virial integrals are of the form

$$\mathcal{W}_{ij} = \rho\Omega_0^2\int_V \Gamma_i x_i x_j\ dV, \tag{2.68}$$

where $\Gamma_i = (3,\ 0,\ -1)$ and the initial minus sign of Equation 2.56 has been factored into Γ. Integrating gives

$$\mathcal{W}_{11} = \frac{m\Omega_0^2}{5}\Big[3a_1^2\cos^2(\theta)+3a_2^2\sin^2(\theta)\Big], \tag{2.69}$$

$$\mathcal{W}_{12} = \frac{m\Omega_0^2}{5}\left[\frac{3}{2}\Big(a_1^2-a_2^2\Big)\sin(2\theta)\right], \tag{2.70}$$

$$\mathcal{W}_{33} = -\frac{m\Omega_0^2}{5}\Big[a_3^2\Big]. \tag{2.71}$$

with the other components being identically zero.

2.2.6 Coriolis force, C_{ij}

The Coriolis term is

$$C_{ij} = 2\rho\Omega\epsilon_{il3}\int_V v_l x_j \, dV, \tag{2.72}$$

where summation over the repeated index l is implied. Using the velocity equations (Equations 2.26 – 2.28) and integrating in the same manner as section 2.2 the non-zero Coriolis terms are obtained,

$$C_{11} = \frac{2}{5}m\Omega_0\left[\frac{1}{2}(\dot{a}_1 a_1 - \dot{a}_2 a_2)\sin(2\theta) + \dot{\theta}\left(a_1^2\cos^2(\theta) + a_2^2\sin^2(\theta)\right) + a_1 a_2\dot{\phi}\right], \tag{2.73}$$

$$C_{22} = \frac{2}{5}m\Omega_0\left[-\frac{1}{2}(\dot{a}_1 a_1 - \dot{a}_2 a_2)\sin(2\theta) + \dot{\theta}\left(a_1^2\sin^2(\theta) + a_2^2\cos^2(\theta)\right) + a_1 a_2\dot{\phi}\right], \tag{2.74}$$

$$C_{12} = \frac{2}{5}m\Omega_0\left[\dot{a}_1 a_1\sin^2(\theta) + \dot{a}_2 a_2\cos^2(\theta) + \frac{1}{2}\dot{\theta}\left(a_1^2 - a_2^2\right)\sin(2\theta)\right], \tag{2.75}$$

$$C_{21} = \frac{2}{5}m\Omega_0\left[-\dot{a}_1 a_1\cos^2(\theta) - \dot{a}_2 a_2\sin^2(\theta) + \frac{1}{2}\dot{\theta}\left(a_1^2 - a_2^2\right)\sin(2\theta)\right]. \tag{2.76}$$

2.3 Equations of Motion

By substituting the results from Equations 2.34–2.37, 2.40–2.43, 2.47, 2.52–2.55, 2.69–2.71, and 2.73–2.76 into the tensor virial theorem equation (Equation 2.4) a set of five coupled ODEs describing the evolution of the cloud is obtained. These equations, corresponding to the 11, 22, 33, 12, and 21 indices are:

$$
\begin{aligned}
&2\ddot{a}_1 a_1 \cos^2(\theta) + 2\ddot{a}_2 a_2 \sin^2(\theta) - \ddot{\theta}\left(a_1^2 - a_2^2\right)\sin(2\theta) = \\
&\quad 2(\dot{a}_1 a_1 - \dot{a}_2 a_2)\left(\dot{\theta} + \Omega_0\right)\sin(2\theta) - 2\dot{\phi}(\dot{a}_1 a_2 - \dot{a}_2 a_1)\sin(2\theta) + 4a_1 a_2 \dot{\phi}\left(\dot{\theta} + \Omega_0\right) \\
&\quad + 2a_1^2\left(\dot{\theta}^2 + \dot{\phi}^2 + 3\Omega_0^2 + 2\Omega_0\dot{\theta} - \frac{3}{2}GmA_1\right)\cos^2(\theta) \\
&\quad + 2a_2^2\left(\dot{\theta}^2 + \dot{\phi}^2 + 3\Omega_0^2 + 2\Omega_0\dot{\theta} - \frac{3}{2}GmA_2\right)\sin^2(\theta) \\
&\quad + 10\left(c_s^2 - \frac{p_{\text{ext}}}{\rho}\right),
\end{aligned}
\tag{2.77}
$$

$$
\begin{aligned}
&2\ddot{a}_1 a_1 \sin^2(\theta) + 2\ddot{a}_2 a_2 \cos^2(\theta) + \ddot{\theta}\left(a_1^2 - a_2^2\right)\sin(2\theta) = \\
&\quad - 2(\dot{a}_1 a_1 - \dot{a}_2 a_2)\left(\dot{\theta} + \Omega_0\right)\sin(2\theta) + 2\dot{\phi}(\dot{a}_1 a_2 - \dot{a}_2 a_1)\sin(2\theta) + 4a_1 a_2 \dot{\phi}\left(\dot{\theta} + \Omega_0\right) \\
&\quad + 2a_1^2\left(\dot{\theta}^2 + \dot{\phi}^2 + 2\Omega_0\dot{\theta} - \frac{3}{2}GmA_1\right)\sin^2(\theta) \\
&\quad + 2a_2^2\left(\dot{\theta}^2 + \dot{\phi}^2 + 2\Omega_0\dot{\theta} - \frac{3}{2}GmA_2\right)\cos^2(\theta) \\
&\quad + 10\left(c_s^2 - \frac{p_{\text{ext}}}{\rho}\right),
\end{aligned}
\tag{2.78}
$$

$$
2\ddot{a}_3 a_3 = -a_3^2\left(3GmA_3 + 2\Omega_0^2\right) + 10\left(c_s^2 - \frac{p_{\text{ext}}}{\rho}\right), \tag{2.79}
$$

$$
\begin{aligned}
&(\ddot{a}_1 a_1 - \ddot{a}_2 a_2)\sin(2\theta) - 2\ddot{\theta}\left(a_1^2 \sin^2(\theta) + a_2^2 \cos^2(\theta)\right) - 2\ddot{\phi} a_1 a_2 = \\
&\quad 4\left(\dot{\theta} + \Omega_0\right)\left(\dot{a}_1 a_1 \sin^2(\theta) + \dot{a}_2 a_2 \cos^2(\theta)\right) + 4\dot{\phi}\left(\dot{a}_1 a_2 \cos^2(\theta) + \dot{a}_2 a_1 \sin^2(\theta)\right) \\
&\quad + a_1^2(\dot{\theta}^2 + \dot{\phi}^2 + 3\Omega_0^2 + 2\Omega_0\dot{\theta} - \frac{3}{2}GmA_1)\sin(2\theta) \\
&\quad - a_2^2(\dot{\theta}^2 + \dot{\phi}^2 + 3\Omega_0^2 + 2\Omega_0\dot{\theta} - \frac{3}{2}GmA_2)\sin(2\theta),
\end{aligned}
\tag{2.80}
$$

$$
\begin{aligned}
&(\ddot{a}_1 a_1 - \ddot{a}_2 a_2)\sin(2\theta) + 2\ddot{\theta}\left(a_1^2 \cos^2(\theta) + a_2^2 \sin^2(\theta)\right) + 2\ddot{\phi} a_1 a_2 = \\
&\quad - 4\left(\dot{\theta} + \Omega_0\right)\left(\dot{a}_1 a_1 \cos^2(\theta) + \dot{a}_2 a_2 \sin^2(\theta)\right) - 4\dot{\phi}\left(\dot{a}_1 a_2 \sin^2(\theta) + \dot{a}_2 a_1 \cos^2(\theta)\right) \\
&\quad + a_1^2(\dot{\theta}^2 + \dot{\phi}^2 + 3\Omega_0^2 + 2\Omega_0\dot{\theta} - \frac{3}{2}GmA_1)\sin(2\theta) \\
&\quad - a_2^2(\dot{\theta}^2 + \dot{\phi}^2 + 3\Omega_0^2 + 2\Omega_0\dot{\theta} - \frac{3}{2}GmA_1)\sin(2\theta).
\end{aligned}
\tag{2.81}
$$

By adding [subtracting] Equation 2.78 to [from] Equation 2.77 the following two relationships are obtained,

$$\begin{aligned}\ddot{a}_1 a_1 + \ddot{a}_2 a_2 = {} & a_1^2\left[\dot{\theta}^2 + \dot{\phi}^2 + 2\dot{\theta}\Omega_0 + 3\Omega_0^2\cos^2(\theta) - \frac{3}{2}GmA_1\right] \\ & + a_2^2\left[\dot{\theta}^2 + \dot{\phi}^2 + 2\dot{\theta}\Omega_0 + 3\Omega_0^2\sin^2(\theta) - \frac{3}{2}GmA_2\right] \\ & + 4a_1a_2\dot{\phi}\left(\dot{\theta} + \Omega_0\right) + 10\left(c_s^2 - \frac{p_{\text{ext}}}{\rho}\right),\end{aligned} \tag{2.82}$$

$$\begin{aligned}(\ddot{a}_1 a_1 + \ddot{a}_2 a_2)\cos(2\theta) - \ddot{\theta}\left(a_1^2 - a_2^2\right)\sin(2\theta) = & \\ 2(\dot{a}_1 a_1 - \dot{a}_2 a_2)\left(\dot{\theta} + \Omega_0\right)\sin(2\theta) - 2\dot{\phi}(\dot{a}_1 a_2 - \dot{a}_2 a_1) & \\ + a_1^2\left[\dot{\theta}^2 + \dot{\phi}^2 + 2\dot{\theta}\Omega_0 - \frac{3}{2}GmA_1\right]\cos(2\theta) + 3a_1^2\Omega_0^2\cos^2(\theta) & \\ - a_2^2\left[\dot{\theta}^2 + \dot{\phi}^2 + 2\dot{\theta}\Omega_0 - \frac{3}{2}GmA_2\right]\cos(2\theta) + 3a_2^2\Omega_0^2\sin^2(\theta). &\end{aligned} \tag{2.83}$$

Similarly, adding [subtracting] Equation 2.80 to [from] Equation 2.81 yields the relationships,

$$\begin{aligned}(\dot{a}_1 a_1 - \dot{a}_2 a_2)\sin(2\theta) + \ddot{\theta}\left(a_1^2 - a_2^2\right)\cos(2\theta) = & \\ - \left(\dot{\theta} + \Omega_0\right)(\dot{a}_1 a_1 - \dot{a}_2 a_2)\cos(2\theta) + 2\dot{\phi}(\dot{a}_1 a_2 - \dot{a}_2 a_1)\cos(2\theta) & \\ + a_1^2\left(\dot{\theta}^2 + \dot{\phi}^2 + 2\dot{\theta}\Omega_0 + \frac{3}{2}\Omega_0^2 - \frac{3}{2}GmA_1\right)\sin(2\theta) & \\ - a_2^2\left(\dot{\theta}^2 + \dot{\phi}^2 + 2\dot{\theta}\Omega_0 + \frac{3}{2}\Omega_0^2 - \frac{3}{2}GmA_2\right)\sin(2\theta), &\end{aligned} \tag{2.84}$$

$$\begin{aligned}\ddot{\theta}\left(a_1^2 + a_2^2\right) + 2\ddot{\phi}a_1 a_2 = & \\ - 2\left(\dot{\theta} + \Omega_0\right)(\dot{a}_1 a_1 + \dot{a}_2 a_2) - 2\dot{\phi}(\dot{a}_1 a_2 + \dot{a}_2 a_1) & \\ - \frac{3}{2}\Omega_0^2\left(a_1^2 + a_2^2\right)\sin(2\theta). &\end{aligned} \tag{2.85}$$

Taking Equation 2.82 and adding [subtracting] Equation 2.84 $\times\sin(2\theta)$ + Equation 2.83 $\times\cos(2\theta)$ yields expressions for $\ddot{a}_1$ and $\ddot{a}_2$,

$$\begin{aligned}\ddot{a}_1 a_1 = {} & a_1^2\left(\dot{\theta}^2 + \dot{\phi}^2 + 2\dot{\theta}\Omega_0 + 3\Omega_0^2\cos^2(\theta) - \frac{3}{2}GmA_1\right) \\ & + 2\dot{\phi}a_1 a_2\left(\dot{\theta} + \Omega_0\right) + 5\left(c_s^2 - \frac{p_{\text{ext}}}{\rho}\right),\end{aligned} \tag{2.86}$$

$$\begin{aligned}\ddot{a}_2 a_2 = {} & a_2^2\left(\dot{\theta}^2 + \dot{\phi}^2 + 2\dot{\theta}\Omega_0 + 3\Omega_0^2\sin^2(\theta) - \frac{3}{2}GmA_2\right) \\ & + 2\dot{\phi}a_1 a_2\left(\dot{\theta} + \Omega_0\right) + 5\left(c_s^2 - \frac{p_{\text{ext}}}{\rho}\right).\end{aligned} \tag{2.87}$$

The equation for $\ddot{a}_3$ is obtained from simplification of Equation 2.79,

$$\ddot{a}_3 a_3 = -a_3^2\left(\frac{3}{2}GmA_3 + \Omega_0^2\right) + 5\left(c_s^2 - \frac{p_{\text{ext}}}{\rho}\right). \tag{2.88}$$

The expression for $\ddot{\theta}$ is obtained through Equation 2.84 $\times \cos(2\theta)$ - Equation 2.83 $\times \sin(2\theta)$,

$$\ddot{\theta}\left(a_1^2 - a_2^2\right) = -2\left(\dot{\theta} + \Omega_0\right)(\dot{a}_1 a_1 + \dot{a}_2 a_2) + 2\dot{\phi}(\dot{a}_1 a_2 - \dot{a}_2 a_1) - \frac{3}{2}\Omega_0^2\left(a_1^2 - a_2^2\right)\sin(2\theta). \tag{2.89}$$

Using this relationship in Equation 2.85$\times\left(a_1^2 - a_2^2\right)$ - Equation 2.89 $\times\left(a_1^2 + a_2^2\right)$ yields the equation for $\ddot{\phi}$,

$$\ddot{\phi}\left(a_1^2 - a_2^2\right) = -2\dot{\phi}(\dot{a}_1 a_1 - \dot{a}_2 a_2) + 2\left(\dot{\theta} + \Omega_0\right)(\dot{a}_1 a_2 - \dot{a}_2 a_1) + 3a_1 a_2 \Omega_0^2 \sin(2\theta). \tag{2.90}$$

Together these 5 coupled ODEs represent the equations of motion (EoM) for the gas cloud.

2.4 Numerical Implementation

It is convenient to adopt unit definitions based on the sound speed of the cloud and the external pressure, with the resulting characteristic length, timescale, mass, and density as,

$$\mathcal{L} = \frac{3c_s^2}{\sqrt{4\pi G p_{\text{ext}}}}, \tag{2.91}$$

$$\mathcal{T} = \frac{3c_s}{\sqrt{4\pi G p_{\text{ext}}}}, \tag{2.92}$$

$$\mathcal{M} = \frac{9c_s^4}{\sqrt{4\pi G^3 p_{\text{ext}}}}, \tag{2.93}$$

$$\rho_{\text{p}} = \frac{3\mathcal{M}}{4\pi\mathcal{L}^3} = \frac{p_{\text{ext}}}{c_s^2}. \tag{2.94}$$

Additionally defined is the magnitude of the tidal force expressed as a density,

$$\rho_{\text{t}} = \frac{9}{4\pi}\frac{\Omega_0^2}{G}, \tag{2.95}$$

which will be used to express the strength of tides relative to the real density, ρ. The tidal density, ρ_{t} is related to the Roche density, ρ_{Roche}, via $\rho_{\text{t}} = \frac{9}{4\times 0.090068}\rho_{\text{Roche}}$ [66].

The singularities apparent in Equations 2.89 and 2.90 when $a_1 = a_2$ deserve examination. One of these singularities can be eliminated by combining the two equations, resulting in

$$\ddot{\phi} + \ddot{\theta} = -\frac{1}{a_1 + a_2}\left[(\dot{a}_1 + \dot{a}_2)\left(\dot{\phi} + \dot{\theta} + \Omega_0\right) + \frac{3}{2}\Omega_0^2(a_1 - a_2)\sin(2\theta)\right], \tag{2.96}$$

which represents the angular acceleration of the internal fluid, when $a_1 = a_2$, and shows that the orbital-frame velocity field is well behaved. This equation is numerically integrated as

opposed to Equation 2.90. The value of $\ddot{\phi}$, representing the fluid sliding with respect to the figure is obtained through subtraction of $\ddot{\theta}$ from this equation. Equation 2.89, specifying $\ddot{\theta}$, is numerically integrated as is, with the singularity, however as will be shown in Section 2.4.1 evolution around the singularity is well-handled by the numerical integrator.

The equations of motion (Equations 2.86 – 2.89 and 2.96), after being normalised as mentioned above, are numerically integrated[1] in the Python programming language using the SunDials [67] numerical integrator module implemented the in scikits ODES [68] package. The relative and absolute errors of the numerical integrator are set to 1×10^{-12} as a middle-ground between speed and accuracy. Appendix B presents computation time vs error threshold graphs in addition to showing the numerical precision loss due to lower specified error tolerances. This work additionally makes use of the software packages and applications listed in Appendix C.

Unless otherwise stated the models are initially in a static equilibrium, $\dot{a}_1 = \dot{a}_2 = \dot{a}_3 = \dot{\theta} = \dot{\phi} = \theta = \phi = 0$. The singularity in Equation 2.89 is avoided by slightly perturbing the equilibrium axes lengths, they are set to $a_1 = 1.005\ \mathrm{r_{eq}}$, $a_2 = \frac{1}{1.005} = 0.995\ \mathrm{r_{eq}}$ and $a_3 = \mathrm{r_{eq}}$, where $\mathrm{r_{eq}}$ represents the equilibrium radius for a Bonnor-Ebert Sphere. The equilibrium radius for a Bonnor-Ebert Sphere of a given mass is obtained by solving the roots of [69]

$$4\pi p_{\mathrm{ext}} r^3 + \frac{3}{5}\frac{Gm}{r} - 3mc_s^2 = 0 \tag{2.97}$$

for a chosen cloud mass, sound speed, and external pressure. Two positive non-zero roots are obtained for each set of parameters, the larger root is taken as it corresponds to the real radius of the cloud [55]—the smaller root corresponds to an unstable Bonnor-Ebert equilibrium point.

2.4.1 Numerical behaviour of singularities

Equations 2.89 and 2.90 exhibit a numerical singularity at $a_1 = a_2$. This singularity arises as the variables θ and ϕ represent the difference in the angle between the unit vectors in the orbital frame and the cloud frame. When the lengths of the cloud's in-plane axes are identical the system becomes degenerate as there is no distinction between the $\hat{x}_1$ and $\hat{x}_2$ directions of the cloud frame. This singularity reflects how small changes in fluid location can result in large changes in θ when $a_1 = a_2$.

When $a_1 = a_2$ the angular velocity of the fluid is given by $\dot{\theta} + \dot{\phi}$, not $\dot{\phi}$. As a result of this, the angular acceleration of the fluid (Equation 2.96), which is well behaved, indicates the velocity, and hence the evolution is also well behaved. Thus, large values of $\ddot{\theta}$ and $\ddot{\phi}$ are physical and the figure can change orientation rapidly when a_1 and a_2 become close while the velocity field need not change much. The numerical integrator's behaviour around the singularity at $a_1 = a_2$ is shown in Figure 2.3, where as the a_1 and a_2 axis lengths of the cloud approach the orientation of the figure (represented by θ) rapidly rotates ≈ 90 degrees while the fluid in the orbital frame does not rotate.

[1] The code used to generate the results is available online at https://github.com/YourLocalBlake/TidalStability

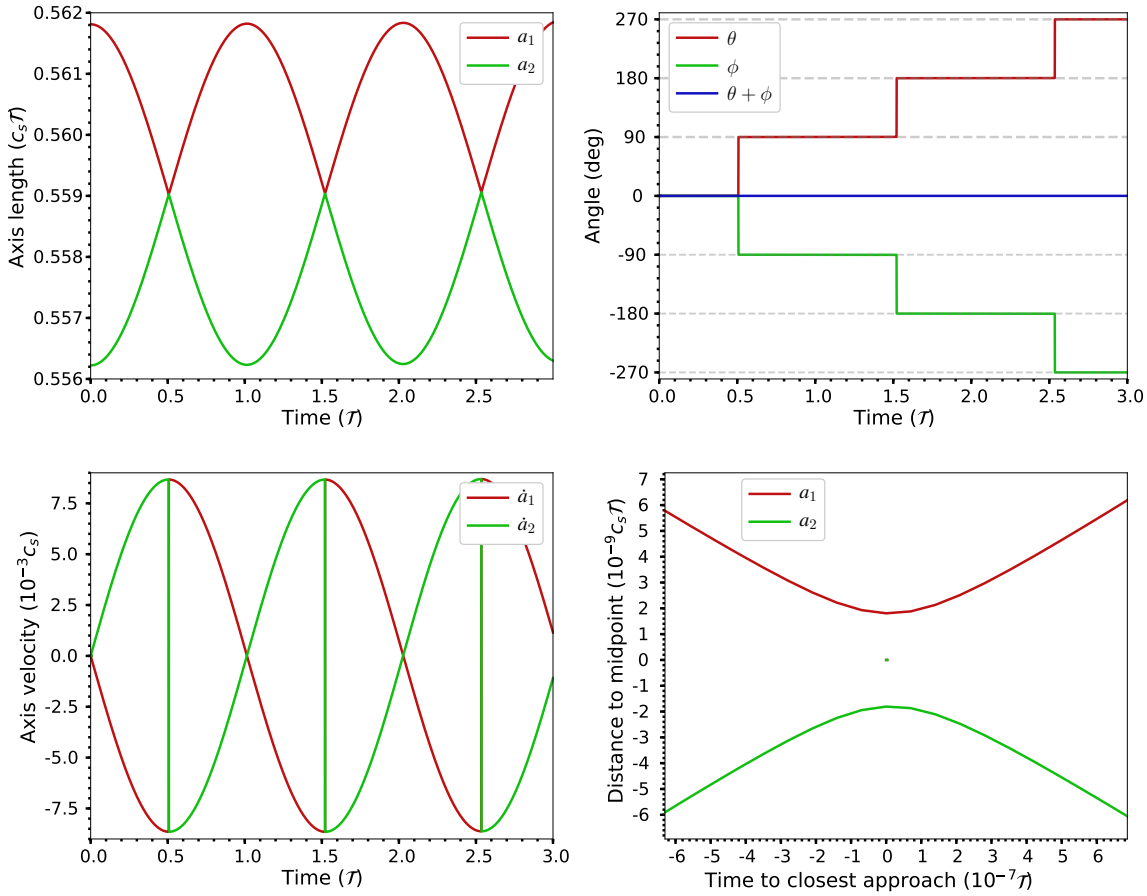

Figure 2.3: Top Left: Evolution of the a_1 and a_2 axes for a Bonnor-Ebert sphere in the absence of tides with $m = m_{\rm BE}$ showing the axes rebound off one another. Top Right: Angles of figure and fluid rotation. Bottom Left: Axes velocities of the cloud showing that the velocities flip as the axes rebound. Bottom Right: Zoomed in version of the top left plot about the first axes rebound. The straight lines are a result of the granularity of time-steps plotted, increasing the number of points plotted results in a smoother curve to the integrator threshold error precision.

An examination of the internal velocity field of the cloud around the time period when the axes rebound off another is shown in Figure 2.4 to further confirm that this behaviour is physical. As the axes approach the cloud figure rotates ≈ 90 deg counter-clockwise, while the major axes rotate ≈ 90 deg clockwise—this behaviour is shown in the second image by the $\hat{\xi}_1$, $\hat{\xi}_2$ unit vectors rotating. The green circle represents a fluid particle on the boundary rotating. Although the fluid particle appears to rotate in the graphs, physically the particle has not changed it's location $[\theta + \phi]$ in space; according to the numerical integrator the black hole is now located on the left. By orientating the axes of the second figure with the first it can be shown that the velocity field of the cloud is identical to before the 'rotations'. This again indicates that the singularity is easily handled by the numerical integrator and that no unphysical abnormalities occur over the time period of the flip.

For the remainder of this thesis the solutions presented will have the axis length values displayed in a manner that represents the physical evolution of the cloud and not the numerical interpretation. This is preformed by swapping the colours of the a_1 and a_2 axes when the numerical integrator has the axes rebound off each other.

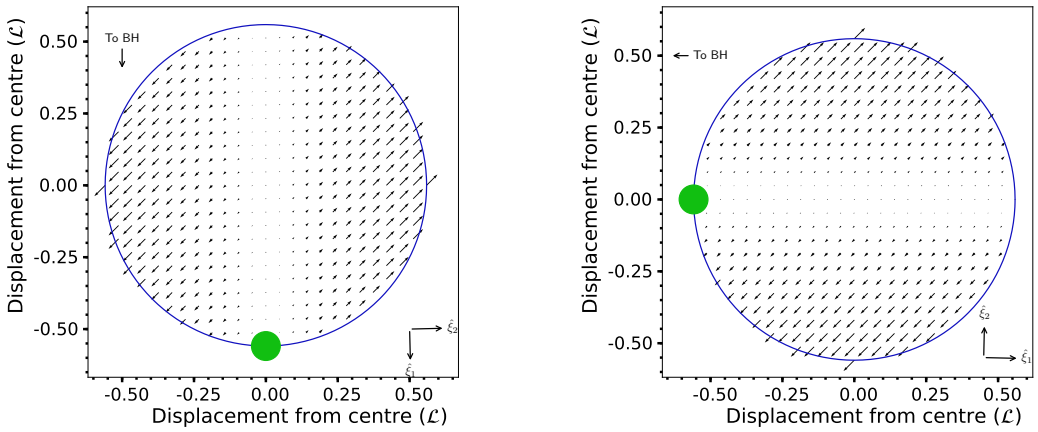

Figure 2.4: Internal velocity field of a Bonnor-Ebert Sphere before and after the a_1, a_2 axes rebound. The magnitude of the arrows between plots are relative. The $\hat{\xi}_1$ orientations relative to the bottom of the figures are 1.38 deg and 88.7 deg in the left and right plots respectively. Orientating the axes of the right and left plot shows that over the axes rebound period the cloud does not physically undergo any violent changes.

2.4.2 Numerical tests

To check the numerical reliability of the results, two numerical tests were undertaken on each calculated solution. The first check is requiring that the solutions satisfy the coupled tensor virial theorem component equations, Equations 2.77 – 2.81, to a specified tolerance level. The evolution of a cloud is calculated and then the solved variables are plugged into the fully coupled equations. By requiring that the difference (relative to zero, representing no error) is less than two orders of magnitude larger than the numerical precision level over the evolution of a solution, an upper-bound of the errors of the model is placed.

The second check is a requirement that analytically constant equations are numerically constant to the specified error tolerance. By considering the equation $\frac{1}{a_1^2-a_2^2}\left(2a_1a_2(2.89) + \left(a_1^2+a_2^2\right)(2.90)\right)$ the relationship

$$2\ddot{\theta}a_1a_2 + \ddot{\phi}\left(a_1^2+a_2^2\right) + 2\dot{\phi}(\dot{a}_1a_1 + \dot{a}_2a_2) + 2\left(\dot{\theta}+\Omega\right)\dot{a}_1a_2 + \dot{a}_2a_1 = 0 \tag{2.98}$$

is obtained, i.e.

$$\frac{d}{dt}\left[2a_1a_2\left(\dot{\theta}+\Omega_0\right) + \left(a_1^2+a_2^2\right)\dot{\phi}\right] = 0. \tag{2.99}$$

Thus, this equation must be constant to the specified error tolerance over the entire solved time period. It was found in the simulation results presented that this equation was constant to the order of magnitude of the specified numerical integrator error tolerance, numerically constant to $\approx 1 \times 10^{-12}$.

3

Tidal stability

This chapter is devoted to firstly, recovering the results and equilibrium solutions of previous work, and secondly, analysis of the effect fluid streaming has on the stability of clouds. To assess the reliability of the derived model Section 3.1 presents solutions in absence of a tidal field, which are compared to known results. Section 3.2 presents the derivation of equilibrium solutions for initially static Roche ellipsoids and pressure-bound Bonnor-Ebert Spheres. Additionally, a comparison of tidal stability to the literature is presented. Following this, in Section 3.3 the equilibrium results are modified to include fluid streaming. A preliminary analysis of the effect fluid streaming has on stability is conducted as well as a brief discussion of the unanswered questions.

The equation for a Bonnor-Ebert Mass, which specifies the limit on the maximum cloud mass that can be in a stable equilibrium, is given by [69]

$$m_{\mathrm{BE}}(p_{\mathrm{ext}}) = \frac{225}{32\sqrt{5\pi}} \frac{c_s^4}{aG^{3/2}} \frac{1}{\sqrt{p_{\mathrm{ext}}}}, \tag{3.1}$$

where a is a constant related to the density distribution of the cloud which has a value of unity for constant spatial density. This chapter focuses on two representative cloud masses: $m = 0.9m_{\mathrm{BE}}$ where self-gravity plays an important role in the stability and evolution, $m = 0.1m_{\mathrm{BE}}$ where self-gravity does not play a crucial role in the clouds dynamics.

3.1 Absence of tides

In the absence of tides the only free parameter of the model is the cloud mass, m/m_{BE}. This results in models where the clouds evolves only with the effects of internal and external pressure, and self-gravity—whose importance to evolution is dictated by the choice of m/m_{BE}. Slightly perturbed quasi-spherical[1] Bonnor-Ebert Spheres were modelled in the absence of

[1] As a result of requiring $a_1 \neq a_2$. See Section 2.4

tides and are shown in Figure 3.1. The axis lengths of the clouds oscillate as expected about their equilibrium position. The system is perturbed through non-equal axis lengths from a stable equilibrium and thus attempts to return to it. Furthermore, the density can be seen to beat from the different periods of oscillations between the a_1, a_2 axes and the a_3 axis, in addition to the a_1 and a_2 axes having different oscillation magnitudes.

These slightly out-of-equilibrium clouds were further perturbed through temporarily increasing p_{ext}. Figure 3.2 shows the result of perturbing the clouds though increasing p_{ext} by 1% for a time period of $0.1\mathcal{T}$—the adopted unit definitions (see Section 2.4) require some variables, e.g. a_1 be scaled such that c_s (equivalently the temperature) remains constant.

It is found that both the $m = 0.1m_{\text{BE}}$ and $m = 0.9m_{\text{BE}}$ clouds begin to oscillate with greater magnitude as a result of the energy injected into the system. Additionally, both clouds beating features, as a result of the magnitude of a_3 oscillations increasing, become more prominent from the increased oscillation magnitudes. Both clouds clouds remain stable as expected.

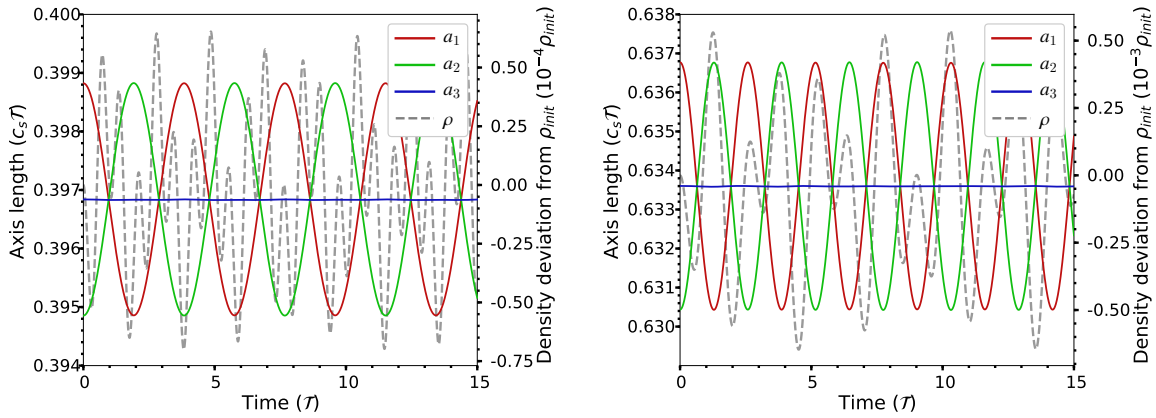

Figure 3.1: Evolution of the axes lengths and density of Bonnor-Ebert Spheres with masses of $m = 0.1m_{\text{BE}}$ (left) and $m = 0.9m_{\text{BE}}$ (right) in the absence of tides.

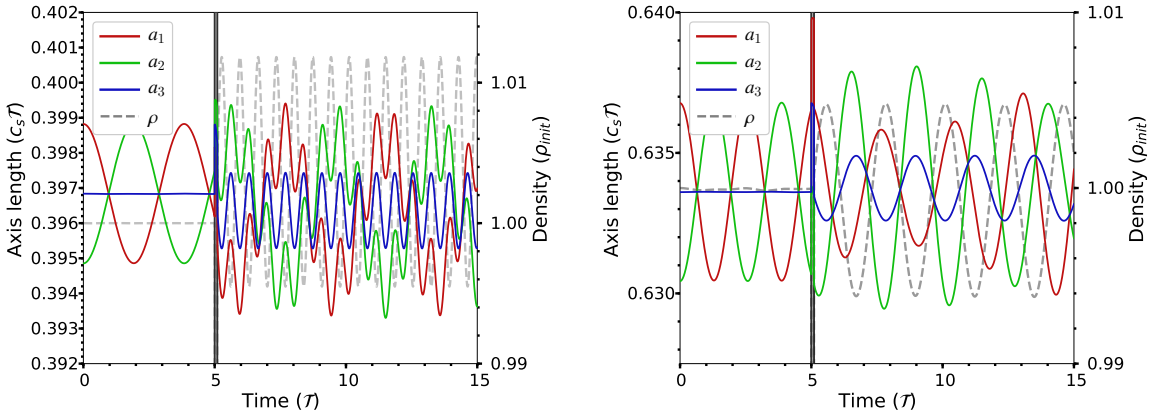

Figure 3.2: Evolution of the axes lengths and density of Bonnor-Ebert Spheres with masses of $m = 0.1m_{\text{BE}}$ (left) and $m = 0.9m_{\text{BE}}$ (right) in the absence of tides. The grey regions represent an increase in p_{ext} by 1% for $0.1\mathcal{T}$ occurring at $\mathcal{T} = 5$. During the increased external pressure period the axis lengths change as a result of rescaling ρ_{p} to be consistent with an increase in external pressure only.

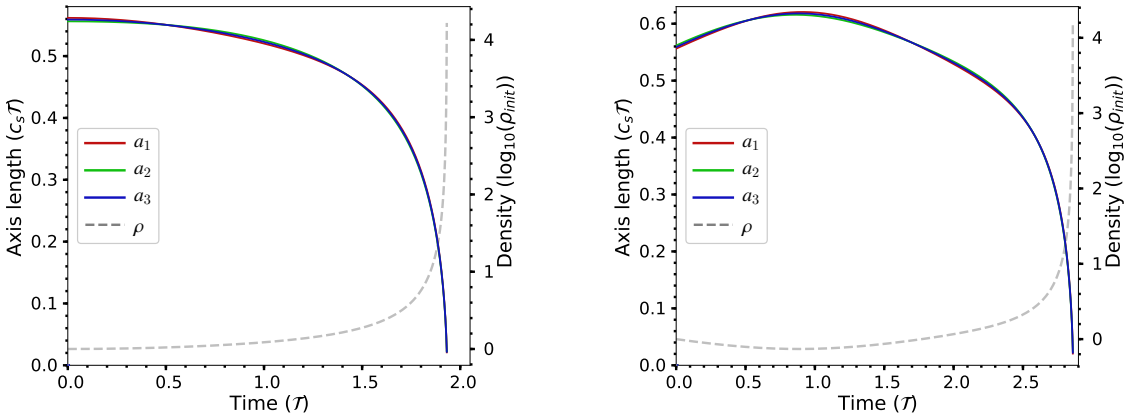

Figure 3.3: Evolution of the axes lengths and density of a $m = 1.01m_{\mathrm{BE}}$ in the absence of tides. Left: Cloud is initially at rest. Right: Cloud is initially expanding in all directions with a rate of 20% the radius of the cloud per unit of time.

Increasing the clouds mass beyond the Bonnor-Ebert Mass (Equation 3.1) should result in a cloud which is gravitationally unstable—resulting in collapse. By considering a cloud of $m = 1.01m_{\mathrm{BE}}$ a gravitationally unstable cloud is modelled. Furthermore, if the cloud is initially expanding outwards it should still collapse. This is because as the clouds expands the force of the external pressure on the cloud increases, which ultimately halts the expansion. Once the cloud has stopped expanding the imbalance between self-gravity, and external and internal pressure will result in the contraction of the cloud. Additionally, as the cloud is more massive than m_{BE} gravitational collapse will occur. The semi-analytical model recovers this behaviour and is shown in Figure 3.3.

3.2 Roche ellipsoid equilibrium solutions

The dependence of ellipsoidal axis ratios on Ω_0^2/ρ for equilibrium solutions of incompressible triaxial-ellipsoids in the absence of external pressures were calculated by Chandrasekhar[66]. As there was no external variable to compare to in his calculations, the physical size (or equivalently, the mass) of the ellipsoids scaled out of the problem. The additional constraint provided by the introduction of external pressure and compressibility fixes the scale of the ellipsoids—which will now be calculated. By choosing an initial axis length ratio, a_3/a_1, the ratio a_2/a_1 can obtained in the same manner as Chandrasekhar, addition of an external pressure makes no difference because it is isotropic. The ratio a_2/a_1 is found through solving the corresponding root of

$$\frac{A_1 a_1^2 - A_3 a_3^2}{A_2 a_2^2 - A_3 a_3^2} - \frac{a_1^2}{a_3^2} - 1 = 0, \tag{3.2}$$

where Equation 3.2 is obtained through the diagonal components of the symmetric tensor virial theorem when no motions are occurring in the system[66]. After obtaining a_2/a_1 the strength of tides can be calculated through[66]

$$\frac{\rho_{\mathrm{t}}}{\rho} = \frac{9}{4\pi}\frac{\Omega_0^2}{G\rho} = \frac{9}{2}a_1 a_2 a_2 \left(\frac{A_1 a_1^2 - A_3 a_3^2}{3a_1^2 + a_3^2}\right). \tag{3.3}$$

Substituting the resulting values into the static case of the 11 component of the tensor virial theorem (Equation 2.86), and choosing a specific cloud density allows the axis length of a_1 to be found through solving the positive root of the equation. This in turn allows for calculation of the physical magnitudes of, respectively, a_2, $a_3 \implies m \implies \rho_t \propto m_{BH}/r_0^3$. Figure 3.4 presents the axis ratio a_2/a_1 and the equilibrium solutions for clouds (in ρ/ρ_t) in terms of the specified input parameter a_3/a_1. Additionally included in this figure are the critical axis ratios calculated by Chandrasekhar[58], C_{max} representing the a_3/a_1 ratio corresponding to the maximum value of Ω_0, and $C_{dissolve}$ corresponding the smallest stable ratio of a_3/a_1 after which instability arises in the clouds due to second-harmonic oscillations[66]. This work finds a similar value for C_{max}, which is not distinguishable when plotted. The grey shaded region in Figure 3.4 represents the Roche limit where it should be noted that no equilibrium configurations exist in this region.

As mentioned above the addition of compressibility and an external pressure allows for unique cloud masses to be associated with tidal strengths. Displayed in Figure 3.5 is the mass of a Bonnor-Ebert Sphere in equilibrium relative to the strength of tides where solutions are plotted as constant ratios of a_3/a_1. The solid lines indicate clouds which are stable to perturbations and the dashed lines indicate unstable clouds by Chandrasekhar's second-harmonic oscillation criterion[66]—the shaded region represents the instability region where no equilibrium configuration exists.

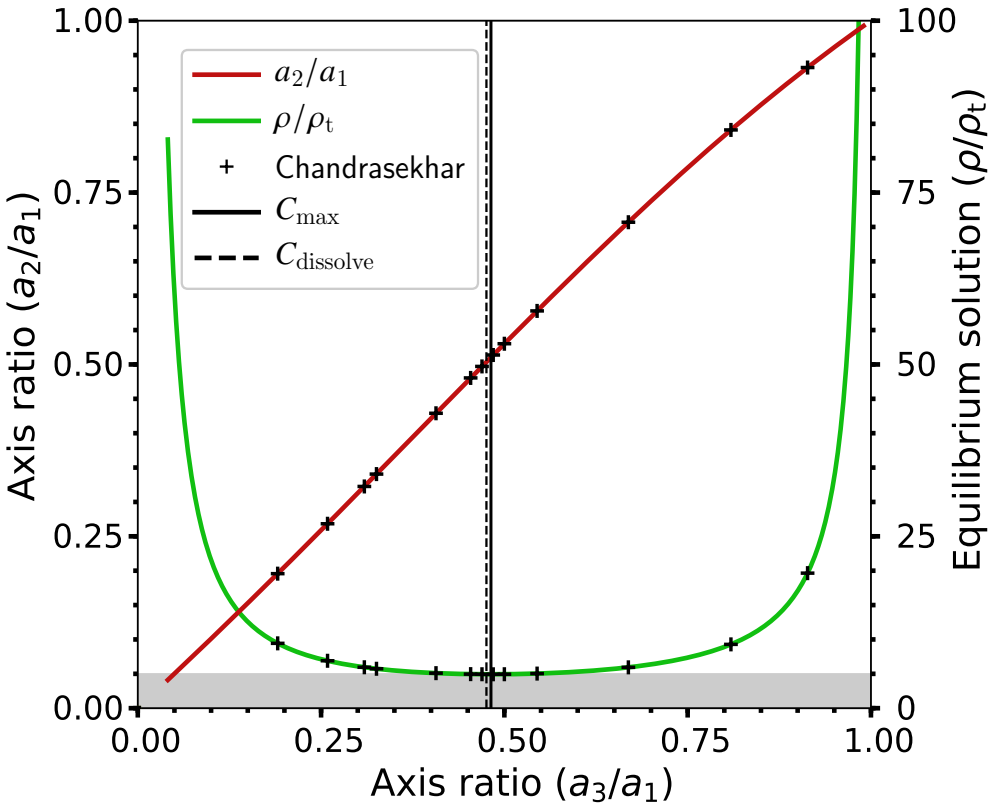

Figure 3.4: Axis length ratios and equilibrium solutions for Bonnor-Ebert Spheres in the presence of a tidal field. + points represent the axis ratio values as calculated by Chandrasekhar[66] in addition to C_{max} and $C_{dissolve}$ which represents the maximum value of Ω_0 for which a equilibrium configuration exists, and the minimum axis ratio for stability to the second-harmonic oscillation criterion. The shaded grey region represents the Roche limit where no equilibriums exist.

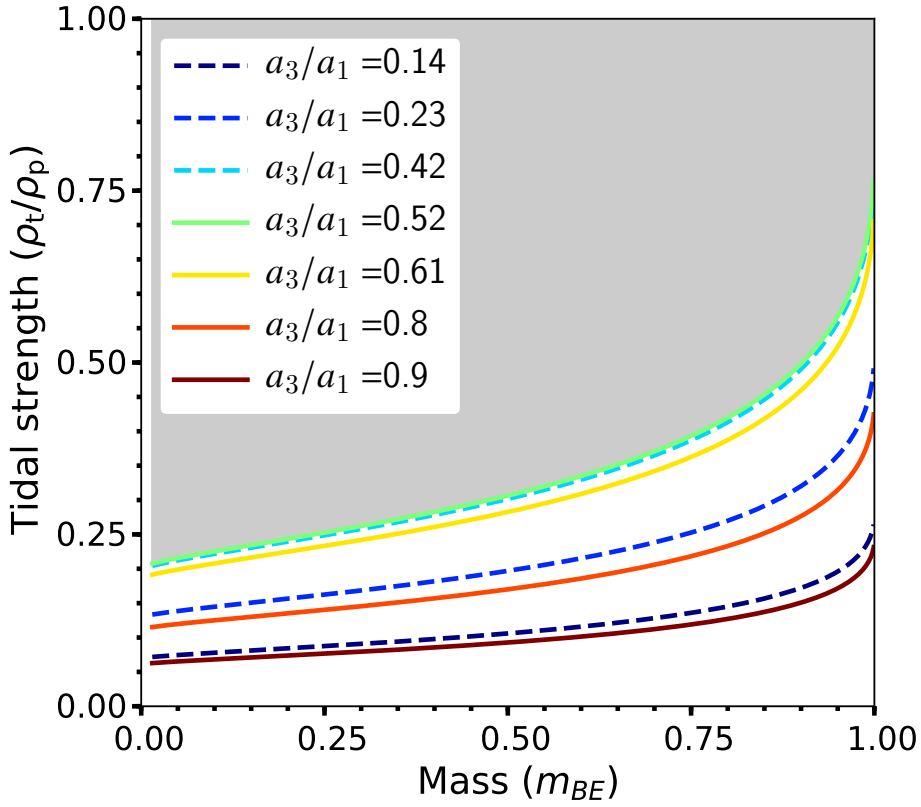

Figure 3.5: Dependence of the axis ratio a_3/a_1 on cloud mass and tidal strength. Solid and dashed lines represent, respectively, stable and unstable equilibria. The shaded grey region contains no equilibria.

To assess the applicabilities of Chandraskar's conclusions, regarding stability, to compressible pressured ellipsoids several clouds were evolved which were subject to a small perturbation away from equilibrium. Models were calculated for an a_3/a_1 axis ratio smaller than C_{dissolve}, between C_{dissolve} and C_{max} and greater than C_{max}. The clouds were perturbed by increasing p_{ext} by 1% for a time period of 1% of a dimensionless orbital period, $\frac{2\pi}{\Omega_0 \mathcal{T}}$. The perturbations to the clouds were performed after one of these dimensionless orbital periods had been completed—this was to assert the equilibrium position is maintained without perturbations. It was found that the clouds to the left of C_{dissolve} and right of C_{max} behaved as expected, i.e. were unstable and stable, respectively. However, the cloud between the two values was unstable to perturbations. Additionally, the $m = 0.9m_{\text{BE}}$ was found to gravitationally collapse along the a_1 axis—in contrast to the other unstable models which all diverged. These models are presented in Figure 3.6.

It is thought the middle-valued $m = 0.1m_{\text{BE}}$ cloud is unstable to perturbations due to its compressibility. This compressibility allows the axis ratios of the cloud to evolve and it is found the density fluctuations lead to axis ratios which are unstable to the second-harmonic criterion. Shown in Figure 3.7 is the axis ratio, a_3/a_1, after the perturbation where the ratio decreases below the second-harmonic oscillation limit, additionally plotted in the top half of the graph is the density and the Roche limit. The $m = 0.9m_{\text{BE}}$ cloud does not display the same behaviour and it is still unclear why the cloud diverges—the $m = 0.9m_{\text{BE}}$ cloud is already gravitationally collapsing before its density exceeds that of a spherical Bonnor-Ebert Mass.

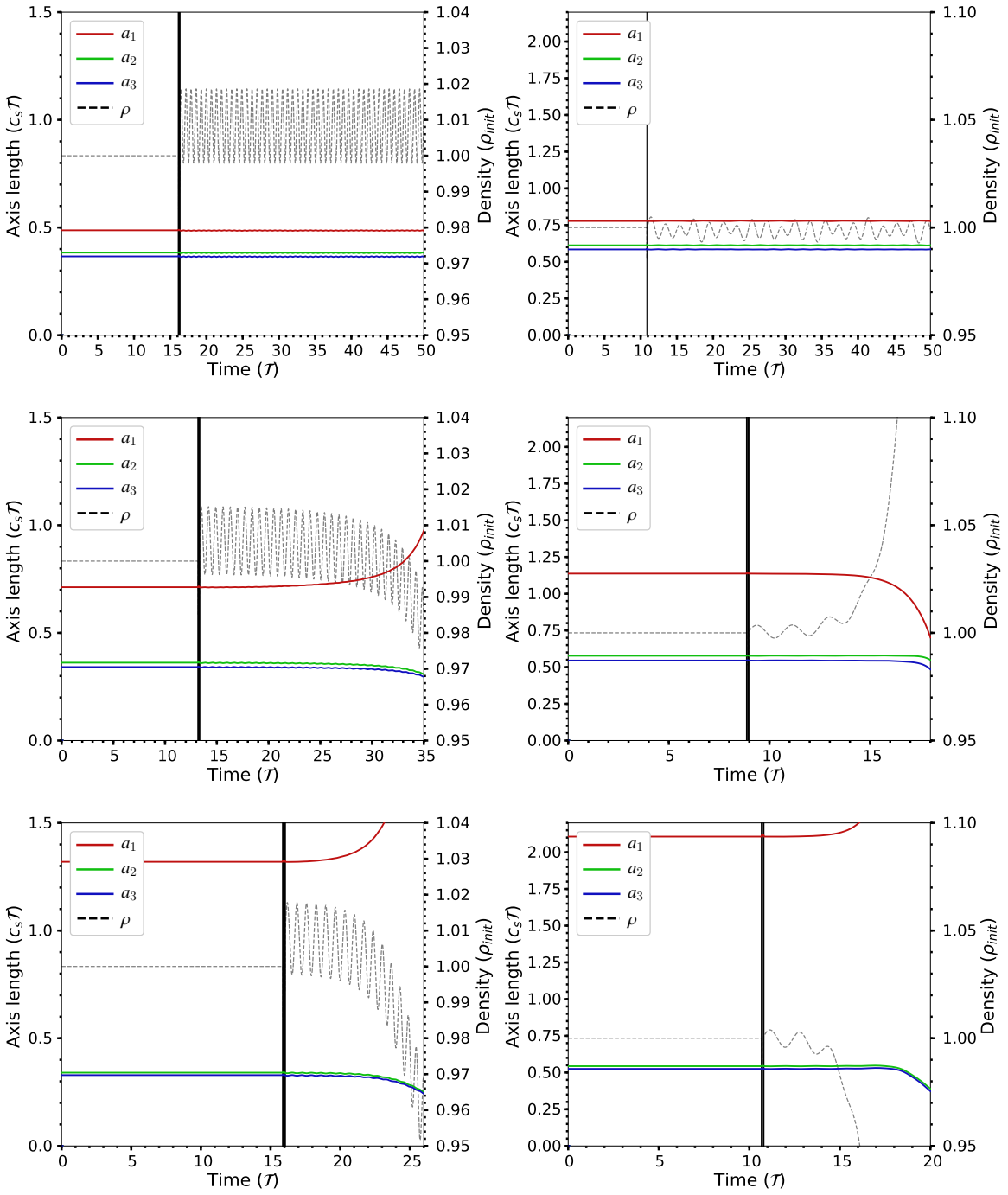

Figure 3.6: Left: Clouds of mass $m = 0.1m_{\mathrm{BE}}$. Right: Clouds of mass $m = 0.9m_{\mathrm{BE}}$. Top: Clouds with $a_3/a_1 = 0.751 > C_{\mathrm{max}}$. Middle: Clouds with $C_{\mathrm{dissolve}} < a_3/a_1 = 0.479 < C_{\mathrm{max}}$. Bottom: Clouds with $a_3/a_1 = 0.249 < C_{\mathrm{dissolve}}$. The grey vertical line represents the period in which the clouds were perturbed by increasing p_{ext} by 1% starting after one dimensionless orbital period $\frac{2\pi}{\Omega_0\mathcal{T}}$ has been completed and lasting 1% of the following orbital period.

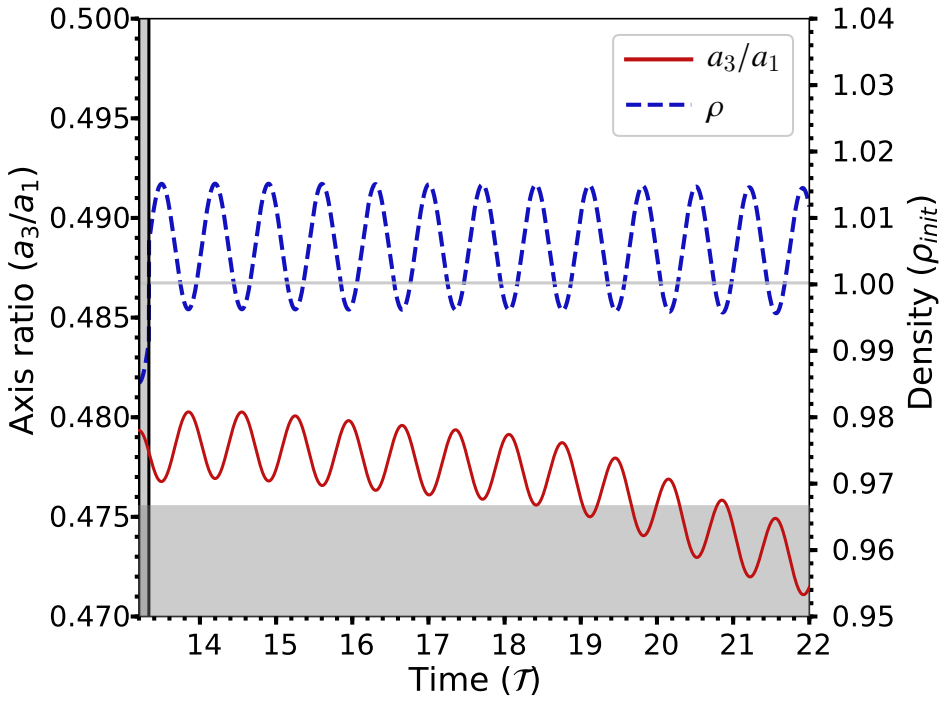

Figure 3.7: Cloud of mass $m = 0.1m_{\rm BE}$ displaying the evolution of the axis ratio a_3/a_1 going below the second harmonic criterion (represented by the grey shaded region) and thus becoming unstable. Additionally shown in the top of the plot is the density of the cloud compared to the Roche limit (horizontal grey line). The grey vertical line at $\mathcal{T} \approx 13$ represents the perturbation.

For completeness the clouds were also perturbed by *decreasing* $p_{\rm ext}$ by 1% for a time period of 1% of a dimensionless orbital period, $\frac{2\pi}{\Omega_0 \mathcal{T}}$. Once again the clouds with a ratio of $a_3/a_1 > C_{\rm max}$ were found to be stable. This clouds with $C_{\rm dissolve} < a_3/a_1 < C_{\rm max}$ where found to be stable and unstable for the $m = 0.1m_{\rm BE}$ and $m = 0.9m_{\rm BE}$ respectively. However, this time the $m = 0.9m_{\rm BE}$ cloud diverged as expected due to violation of the second-harmonic criterion. The $m = 0.9m_{\rm BE}$ cloud with $a_3/a_1 < C_{\rm dissolve}$ was found to gravitationally collapse, the cause of which is still unknown. The $m = 0.1m_{\rm BE}$ cloud with $a_3/a_1 < C_{\rm max}$ was initially enigmatic as it was also found to stably oscillate. This result is thought to be physical because this form of perturbation has compressed the originally pressure-bound cloud which was initially in equilibrium, removing the compressive force results in the cloud wanting to expand—thus leading to the oscillations. The figures showing the evolution of these clouds are presented in Figure 3.8.

As explored in the preceding paragraphs, the equilibrium positions in the presence of strong tides are close to oblate ellipsoids with a $2-1$ axis ratio. Before exploring the effects of internal fluid slippage, another reliability assessment of the model is conducted. Quasi-spherical Bonnor-Ebert Spheres were modelled near the Roche limit analogous to geometric perturbations from the equilibrium solution. The models in this thesis, although compressible, should still disrupt close to the Roche limit (as the are significantly geometrically perturbed from the equilibrium position). Shown in Figure 3.9 are these geometrically perturbed clouds. As expected, when the clouds are moderately far away from the Roche limit they oscillate wildly, due to the tidal field and displacement from equilibrium, and when the Roche limit is exceeded the clouds are torn apart—as expected.

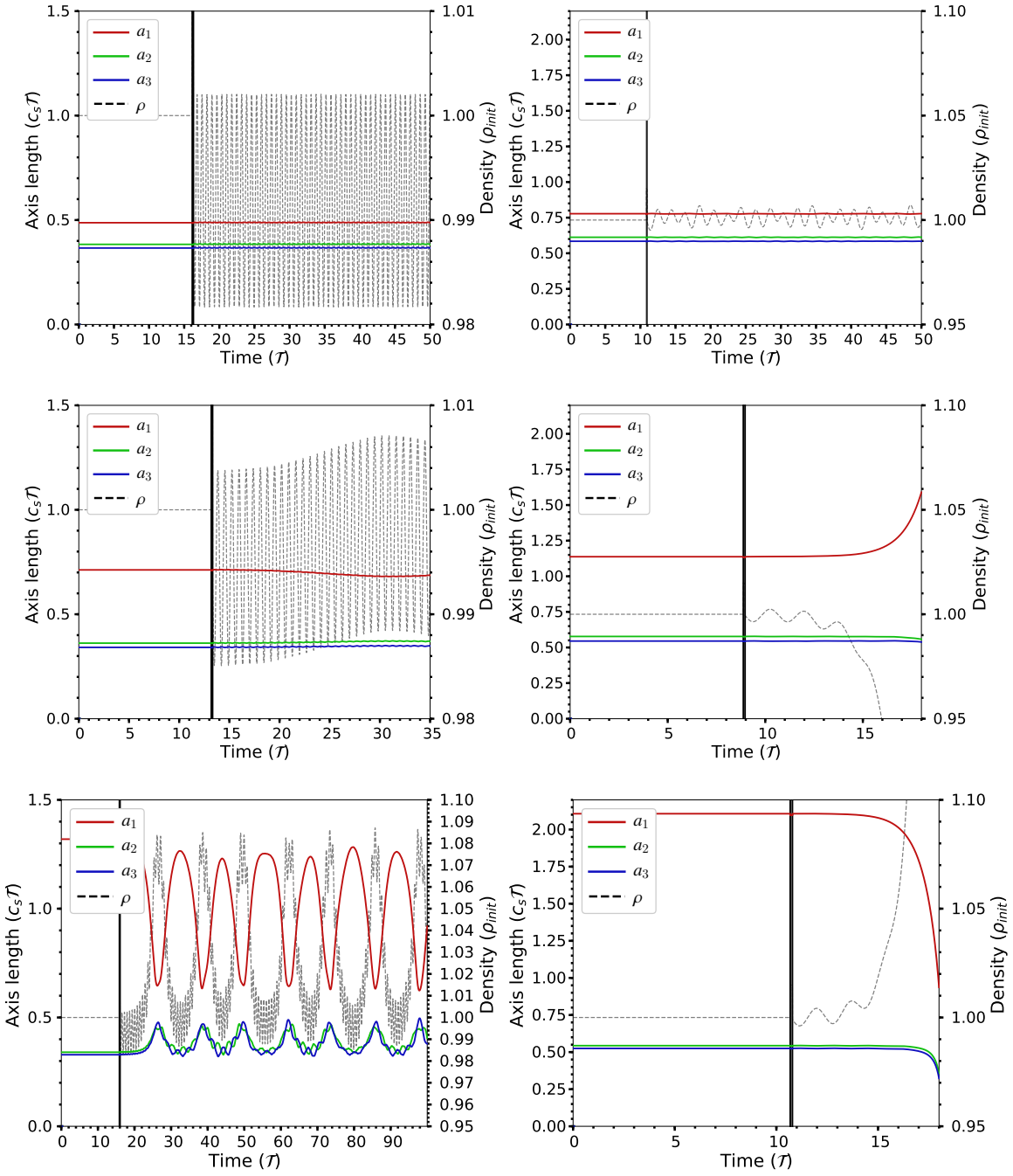

Figure 3.8: Left: Clouds of mass $m = 0.1m_{\mathrm{BE}}$. Right: Clouds of mass $m = 0.9m_{\mathrm{BE}}$. Top: Clouds with$a_3/a_1 = 0.751 > C_{\mathrm{max}}$. Middle: Clouds with $C_{\mathrm{dissolve}} < a_3/a_1 = 0.479 < C_{\mathrm{max}}$. Bottom: Clouds with $a_3/a_1 = 0.249 < C_{\mathrm{dissolve}}$. The grey vertical line represents the period in which the clouds were perturbed decreasing ρ_{norm} by 1% starting after one dimensionless orbital period has been completed and lasting 1% of the following period.

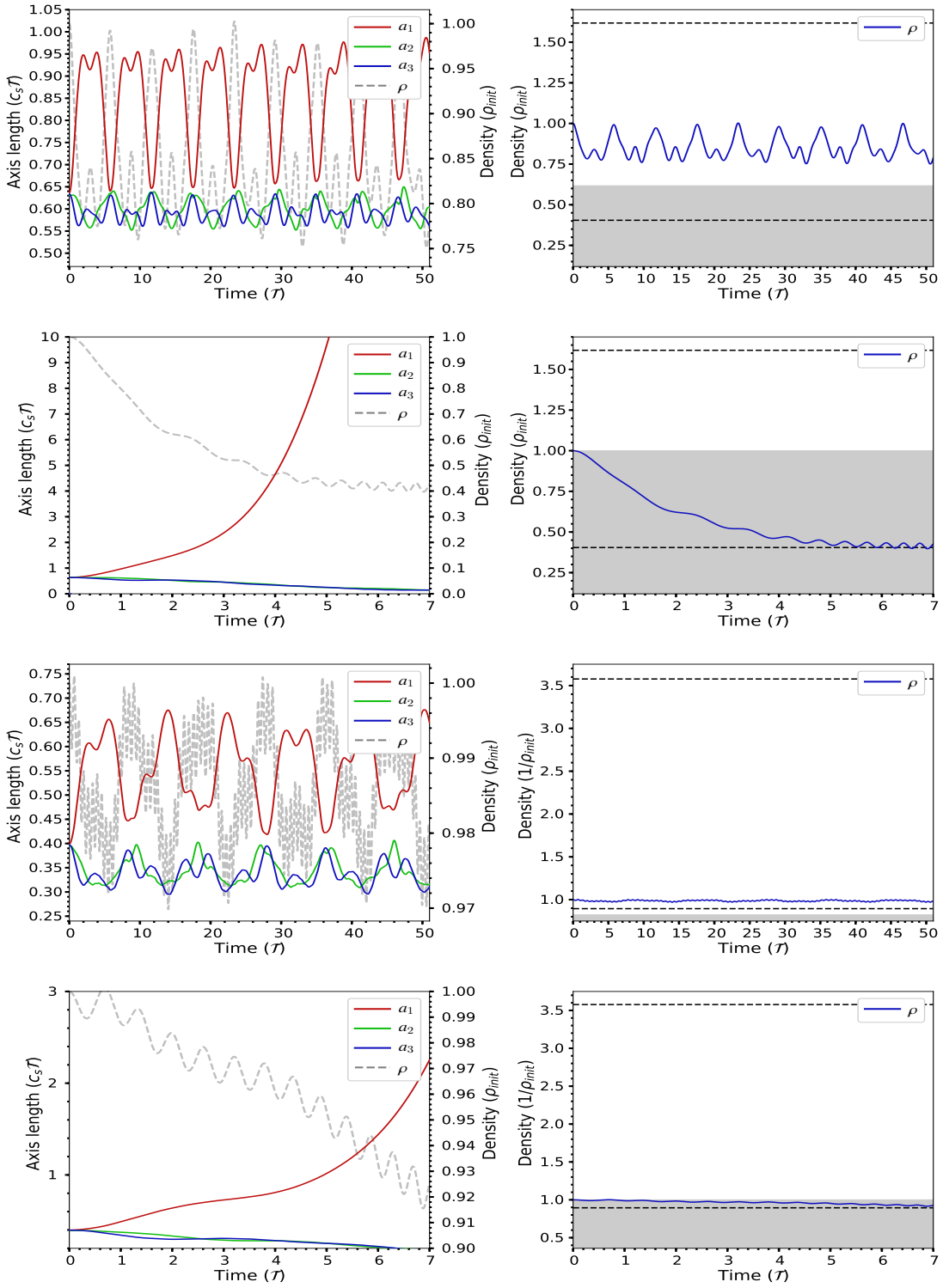

Figure 3.9: The top 4 panels show the evolution of a cloud of mass $m = 0.9m_{\rm BE}$ and the bottom 4 panels show the evolution for a mass of $m = 0.1m_{\rm BE}$. Left: Axes length evolution of a Bonnor-Ebert sphere in the presence of moderate strength tidal fields (1st and 3rd) and with a tidal field consistent with placing the cloud at the Roche limit (2nd and 4th). Right: The density of the clouds compared to the Roche limit, shown in grey. The top black dashed line represents a density of $m = m_{\rm BE}$ which should the cloud exceed is unstable to self-induced gravitational collapse; the bottom black line represents the density equivalent to the limit as $m \to 0$.

3.3 Internal streaming

We now consider the evolution of an initially static pressure-bound sphere with fluid streaming. Physically, the streaming allows the gas to flow separately from changes to the geometry of the cloud e.g. stretching, compression, and orientation of the major axes of the ellipsoid. A gas cloud can be statically stretched towards the black hole and with it's major axes aligned with the orbital frame axes ($\theta = 0$) but with the fluid of the cloud streaming with the figure while preserving the shape. This is physically motivated as tidal locking is not expected due to the low viscosity of the clouds.

By seeking an equilibrium in which the axes length are not changing in time, self-gravity is negligible ($m \ll m_{\rm BE}$), with no figure rotation, and allowing for internal fluid slippage at a fixed rate ($\dot{\phi}$ = constant) the EoM (Equations 2.86 – 2.90) reduce to three non-zero equations:

$$0 = a_1^2\left(\dot{\phi}^2 + 3\Omega_0^2\right) + 2\Omega_0 a_1 a_2 \dot{\phi} + 5\left(c_s^2 + p_{\rm ext}/\rho\right), \tag{3.4}$$

$$0 = a_2^2\left(\dot{\phi}^2\right) + 2\Omega_0 a_1 a_2 \dot{\phi} + 5\left(c_s^2 + p_{\rm ext}/\rho\right), \tag{3.5}$$

$$0 = -a_3^2\left(\Omega_0^2\right) + 5\left(c_s^2 + p_{\rm ext}/\rho\right). \tag{3.6}$$

Subtracting Equation 3.5 from Equation 3.4 and dividing by a_1^2 yields the first axis length relationship,

$$\left(\frac{a_2}{a_1}\right)^2 = 1 + \frac{3}{\alpha^2}, \tag{3.7}$$

where $\alpha = \dot{\phi}/\Omega_0$. Substituting this relationship into Equation 3.5 and subtracting Equation 3.6 yields

$$\left(\frac{a_3}{a_1}\right)^2 = -\left(3 + \alpha^2\right) - 2\sqrt{3 + \alpha^2} \times \mathrm{sgn}(\alpha). \tag{3.8}$$

Requiring that this ratio be real valued implies that

$$-1 < \alpha < 0, \tag{3.9}$$

i.e. $-\Omega_0 < \dot{\phi} < 0$. This is suggestive that an equilibrium solution in the presence of a strong tidal field exists when a cloud has counter-rotating internal fluid. However, inspection of equations 3.7 and 3.8 shows that for low rotation rates $a_2 \gg a_1$ and as $\dot{\phi}$ approaches Ω_0 the a_3 axis length reduces to zero—these wildly distorted ellipsoids pose a serious question about their stability in the presence of strong tides. The solutions of the a_1 axis length were obtained through the following procedure—which is similar to Section 3.2. Firstly, a fixed value of α is chosen and the axis length ratios are obtained through Equations 3.7 and 3.8. Following this, a specific value of Ω_0 and ρ is chosen. These values and axis ratios are then substituted into Equation 3.6 which has previously been divided by a_1^2, to obtain an equation in a_1 from which the value is numerically found through a root solving routine.

3.3.1 Stability

To assess the effect internal streaming has on the stability of the clouds two values of α, -0.1 and -0.5, were chosen to be investigated. The axis lengths corresponding to these values of α were used as an initial guess for a self-gravitating cloud with mass $m = 0.01 m_{\rm BE}$ for a multi-dimensional root finding algorithm which was solving the complete set of the EoM (Equation 2.86 – 2.90). The equilibrium semi-axes were obtained, the mass was then increased slightly ($\approx 0.001 m_{\rm BE}$), and the new equilibrium lengths calculated—this process was repeated until the desired mass was obtained. Shown in the left panel of Figure 3.10 are the equilibrium axes lengths obtained.

The root solver was temperamental. Because, there exists at least two strictly positive equilibrium solutions with fluid streaming—the root solver jumped between these solutions, occasionally converging to unphysical (negative) roots for the axes lengths. A strict thesis deadline prevented full investigation of this behaviour. Shown in the right panels of Figure 3.10 are the other two physical equilibrium solutions found. The right panels of Figure 3.10 additionally show the unreliable results for masses below $0.1 m_{\rm BE}$ where the root finder has discontinuities in the curves. The $0.1 m_{\rm BE}$ solutions found appear reliable, it was confirmed these equilibria were real through substituting the values into the full EoM (Equations 2.86 – 2.90), where it was checked that these solutions remained static unless perturbed.

The right panel of Figure 3.10 shows that the smaller equilibria solution set appears not to depend significantly on the choice of α. This behaviour was investigated and is shown in Figure 3.11 where it is seen these axis lengths do not vary much over the range of α values. Equilibrium solutions for sample values of α were calculated, represented by the points on the plot; the curves are interpolated. The smaller solutions appear to contain an approximate $2-1$ axis ratio, $2a_1 \approx a_2 \approx a_3$. This ratio is oddly suggestive of the $2-1$ equilibria solutions of the Roche ellipsoids near the Roche density when $\alpha = 0$ (See Figure 3.4)—this possible connection will be investigated in future work.

Interestingly to note is that highly distorted clouds, shown on the left of Figure 3.10, have a_2, the in-plane orbital axis orthogonal to the tidal force, as the longest axis; this is different from the smaller equilibria, which is consistent with the finding of Chandrasekhar presented in Section 3.2, where a_1, the axis directed towards the black hole is the longest. It is thought the large a_2 axis length could be a result of the cancelling of the tidal force by the centrifugal force (Section 2.2.5) which creates the asymmetry in Equations 3.4 and 3.5 and leads to the significant deviation from sphericity.

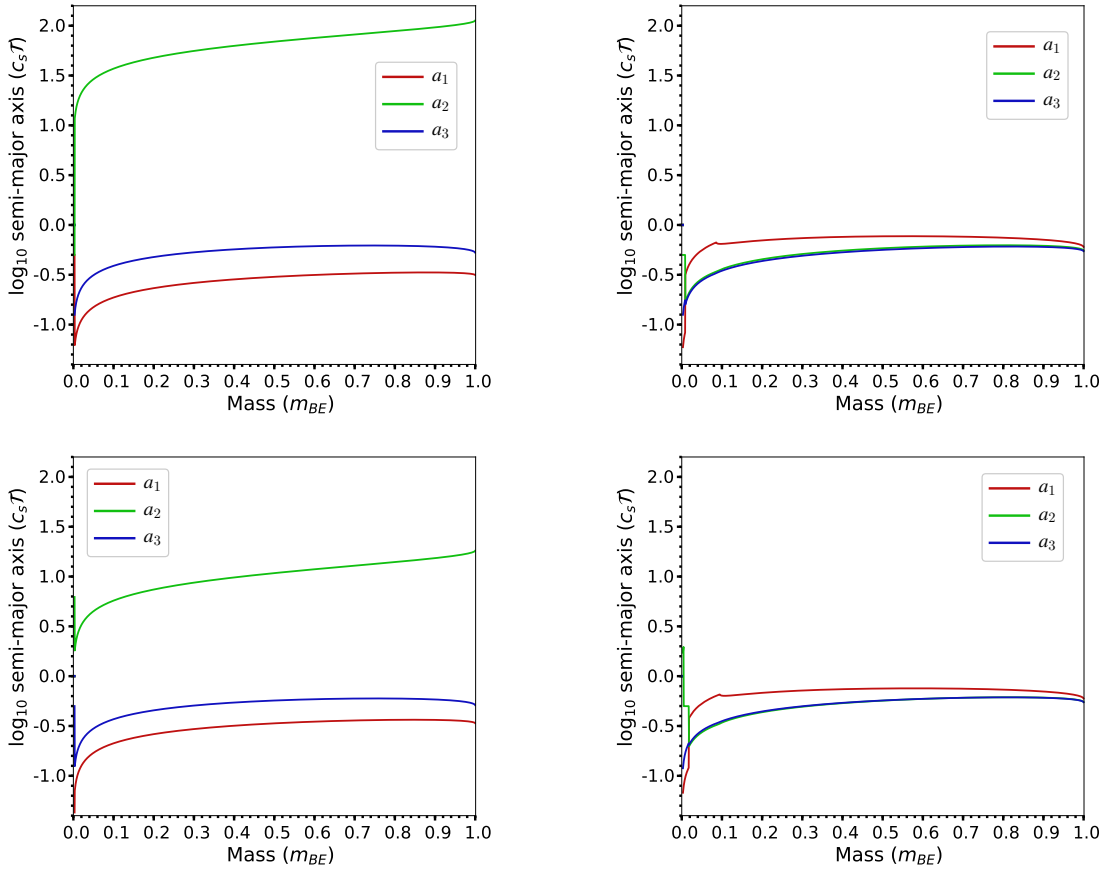

Figure 3.10: The equilibrium axes lengths for a Bonnor-Ebert Spheres for varying mass, with $\alpha = -0.1$ (top panels), and $\alpha = -0.5$ (bottom panels). Two plots (left and right panels) are shown for each of the α values as two unique solutions were found in each case. The lines represent the equilibrium solutions. The values near $m = 0$ have been plotted to show the instability of solutions with masses below $0.1m_{\rm BE}$.

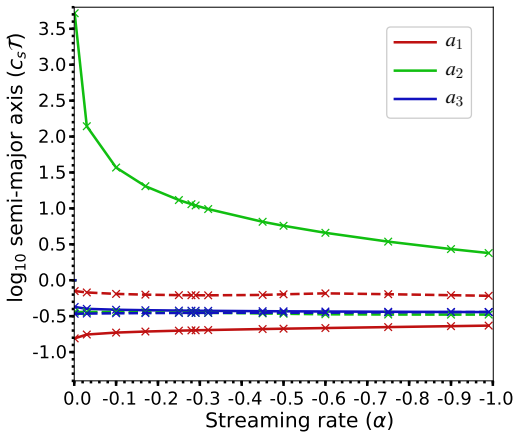

Figure 3.11: Equilibrium axis lengths for Bonnor-Ebert Spheres with $m = 0.1m_{\rm BE}$ and varying α values. The solid and dashed lines represent the two different physical equilibria solution sets found by the root solver.

3.3.2 Violation of the Roche limit

The impact of fluid streaming on the stability and equilibrium configurations of pressure-bound self-gravitating Bonnor-Ebert spheres with densities slightly below the Roche density were investigated. The two equilibria solutions for a cloud with mass ($m = 0.1 m_{\rm BE}$) were obtained as specified in Section 3.3.1. The evolution of these clouds was then subject to a temporary increase in external pressure, as in the preceding sections. The results are presented in Figure 3.12. The compactor equilibria solution oscillates stably. Additionally, the densities oscillate even further below the Roche density, violating the criterion, even more severely, than the initial equilibrium.

As the clouds oscillate, in addition to the size of the smaller equilibria clouds not varying significantly with a change in α, suggests the internal streaming may have a more dynamic effect on the stability of the clouds—not an initial effect on the geometry. This could similar to the epicyclic motion in disks. As a result of this, and the approximate axis ratio of a Roche ellipsoid, future work will investigate the effect of the streaming velocity on the evolution of Roche ellipsoids. Additionally, the observed stability that the counterrotating fluid provides to the smaller equilibria solutions suggests rotation has a significant effect of the stability of the clouds. After a more thorough investigation of this effect, if this rotation is found to play a substantial role, then a model allowing for fluid streaming in three dimensions (opposed to the restricted two dimensional in-plane rotation of this model) will be formulated and the effects characterised.

The clouds with larger axis lengths, as shown in Figure 3.11, collapse as a result of the perturbation. This is suggestive of the unstable equilibrium axis length which for varying mass values is highly gravitationally unstable. This is believed to be consistent with the two equilibrium radii for quasi-spherical Bonnor-Ebert Spheres where one radius is stable, and the other is an unstable equilibrium point. This instability is additionally physically motivated as the a_2 axis is at least an order of magnitude larger than the other axes and hence is widely distorted from a sphere - the distortion is easily seen in the bottom panels of Figure 3.12.

An investigation into the equilibrium solutions and stability of differing density clouds, with a wider range of α values (including the $\alpha = 0, -1$ limits), and in the presence of stronger tides is left for future work.

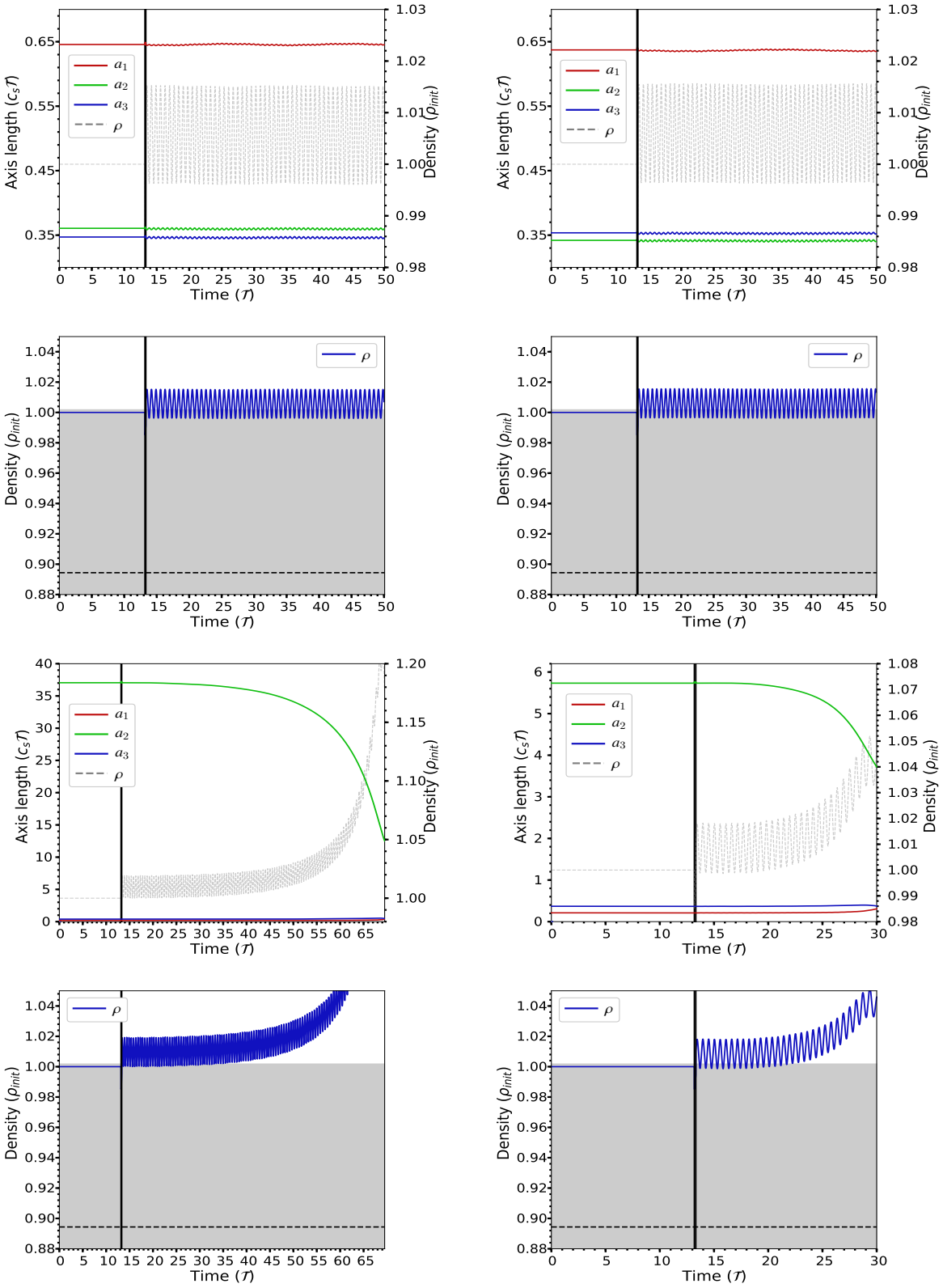

Figure 3.12: Evolution of $m = 0.1 m_{\rm BE}$ Bonnor-Ebert Spheres with internal streaming and initially violating the Roche density, $\rho < \rho_{\rm Roche}$. Left: $\alpha = -0.1$. Right: $\alpha = -0.5$. Top two rows: The smaller equilibrium axis set from Figure 3.10 with the top panels displaying the axis evolution and the bottom panels displaying the density compared to the Roche Density (Shaded region). Bottom two rows: The same as above except using the larger equilibrium set values. The vertical line indicates the time of perturbation and the dashed bottom black line represents the density equivalent to the limit as $m \to 0$.

4

Discussion and conclusion

This research was motivated by the emerging evidence of low mass star formation with several parsecs of the Galactic centre. A semi-analytic approach was undertaken to model the evolution of an isothermal compressible tri-axial ellipsoid characterising a Bonnor-Ebert sphere in the presence of tides; physically corresponding to self-gravitating gas clouds embedded in a high pressure medium under the influence of a black hole, such as at the Galactic centre. The derivation of the equations of motion for the cloud with an approximation of constant spatial density, but with a linear velocity field consistent with the cloud's figure, and allowing internal streaming of fluid were presented. The accompanying tensor virial theorem integrals were evaluated to obtain the 2nd order coupled ODES for the evolution of the semi-axes, orientation, and velocity field. The results are as follows:

1. The model reproduces expected behaviour of Bonnor-Ebert spheres—where perturbations led, to oscillations, collapse, or expansion as predicted.

2. The reproduction of Chandrasekhar's results regarding the equilibrium configurations of ellipsoids subject to tidal fields, and the confirmation of stability to the second-harmonic oscillation criterion. Both which provide validation and confidence for the model and approach.

3. The extension of Chandrasekhar's equilibrium configuration, whereby the introduction of the new elements of compressibility and external pressure allowed for axis ratios and densities to be obtained as a function of Bonnor-Ebert mass—obtaining a unique physical mass-size-shape relationship for a given tidal strength, where increasing the mass results in greater stability.

4. Two new classes of equilibrium solutions with internal streaming were discovered, showing rotation has a significant effect on stability. One class, characterised by $a_2 \gg a_1,\ a_3$ proved to be unstable. The other class was stable and more compacted, with $2a_1 \approx a_2 \approx a_3$. The low masses had $\rho < \rho_{\text{Roche}}$, and merit further investigation.

The violation of the Roche limit for stable low ($m = 0.1 m_{\rm BE}$) mass Bonnor-Ebert spheres with internal fluid streaming occurs in the presence of moderate tides $\rho_{\rm Roche} \sim 1.15 p_{\rm ext}/c_s^2$ Applying this to the central few parsecs of the galaxy, adopting an external pressure of $\sim 1.5 \times 10^9\,{\rm K\,cm^{-3}}$, and a cloud sound speed of $c_s \sim 0.6\,{\rm km\,s^{-1}}$ (cloud temperature = 100 K), implies a Bonnor-Ebert mass of $\sim 1.5\,{\rm M}_\odot$. Additionally it leads to a characteristic length of $c_s \mathcal{T} \sim 0.0084\,{\rm pc} = 1732\,{\rm AU}$. Which applied to Sgr A* yields a distance to the Roche limit of 2.5 pc. This is too large to be immediately relevant to the emerging evidence for star formation at 0.1–1 pc, but it is likely that these solutions exist for stronger tides (larger $\rho_{\rm t}$ or $\rho_{\rm Roche}$), and this is an avenue for future research.

While the results do not yet solve the disparity between observation of stable dense gas clouds in the Galactic centre and theory it is, in the author's opinion, that the solution lies in a more thorough analysis of effect of rotation. It is evident there was significant numerical problems hindering a complete analysis on the effects rotation has on the stability of clouds. In addition, a better characterisation of the strength of the pressure in the galactic centre, such as the effect of turbulence in the clouds, is thought to aid stability and help explain the observations.

The main limitations in the model are the approximation of constant density and the lack of substructure information as a result of the virial technique. While the CNR shows 'clumpiness' in it's structure and clouds cores are known to be centrally concentrated the approximation of constant density only yields weaker self-gravity. The effect is negligible in the results presented in the latter section of this work—models applicable to the clouds in the Galactic centre—where the choice of $m = 0.1 m_{\rm BE}$ creates clouds where the contribution from self-gravity is small compared to the other competing forces. Additionally, the model presented describes a monolithic evolution of a cloud. This is sufficient for the investigation undertaken in this work as fluctuations on the smaller scale are arguable less important in maintaining the tidal stability of the clouds with respect to the black hole than the competition between tides and external pressure.

There are several future prospects for this work which could not be initially carried out in this work. Firstly, a more robust root finding method needs to be developed and applied to low mass clouds. While the single-dimensional roots are quickly and accurately obtained through an implementation based on Muller's method[70] the multi-dimensional roots pose a significant problem. The current implementation uses algorithms such as hybr—a modified Powell method[71], and Broyden[72] methods as the back-end to find the roots. Future work aims to implement the equations in a numerically simpler form, with higher numerical resolution, aided by non-restrictive time-restrains to obtain roots for varying streaming velocities. Which, in addition to a broader range of streaming velocities, will allow for a wider exploration of the equilibrium and stability effects internal streaming can have on the stability of clouds. This will allow for analysis of stronger tidal fields, and further possible violation of the Roche limit for varying cloud masses. A more general description of the cloud's dynamics will be derived, where the internal fluid and figure orientation can vary in all three dimensions with respect to the black hole. Work will be continued into the effects of dynamic processes on the cloud, i.e. time-varying tidal fields resulting from elliptic orbits, and varying external pressures which can model its evolution of dynamic effects e.g. turbulence inside the CNR. This will allow for more comprehensive analysis into cloud collapse around Sgr A* and hence star formation in the centre of galaxies.

A

Inertia tensor derivation

The left-hand-side of the tensor virial theorem (Equation 2.4) is

$$\dot{\mathcal{H}}_{ij} = \frac{d}{dt}\int_V \rho v_i x_j \, dV. \tag{A.1}$$

Substituting the relations from Equations 2.11 and 2.26–2.28 for x_j and v_i in Equation A.1 yields the five components:

$$\begin{aligned}\dot{\mathcal{H}}_{11} = \frac{d}{dt}\int_V \rho \Bigg[& \xi_1^2 \cos(\theta)\left(\frac{\dot{a}_1}{a_1}\cos(\theta) - \sin(\theta)\left(\dot{\theta} + \frac{a_2}{a_1}\dot{\phi}\right)\right) \\ & - \xi_2^2 \sin(\theta)\left(-\frac{\dot{a}_2}{a_2}\sin(\theta)\right) - \cos(\theta)\left(\dot{\theta} + \frac{a_1}{a_2}\dot{\phi}\right)\Bigg] dV,\end{aligned} \tag{A.2}$$

$$\begin{aligned}\dot{\mathcal{H}}_{22} = \frac{d}{dt}\int_V \rho \Bigg[& \xi_1^2 \sin(\theta)\left(\frac{\dot{a}_1}{a_1}\sin(\theta) + \cos(\theta)\left(\dot{\theta} + \frac{a_2}{a_1}\dot{\phi}\right)\right) \\ & + \xi_2^2 \cos(\theta)\left(\frac{\dot{a}_2}{a_2}\cos(\theta)\right) - \sin(\theta)\left(\dot{\theta} + \frac{a_1}{a_2}\dot{\phi}\right)\Bigg] dV,\end{aligned} \tag{A.3}$$

$$\dot{\mathcal{H}}_{33} = \frac{d}{dt}\int_V \rho \left[\xi_3^2 \frac{\dot{a}_3}{a_3}\right] dV, \tag{A.4}$$

$$\dot{\mathcal{H}}_{12} = \frac{d}{dt}\int_V \rho\left[\xi_1^2\cos(\theta)\left(\frac{\dot{a}_1}{a_1}\sin(\theta)+\cos(\theta)\left(\dot{\theta}+\frac{a_2}{a_1}\dot{\phi}\right)\right) - \xi_2^2\sin(\theta)\left(\frac{\dot{a}_2}{a_2}\cos(\theta)-\sin(\theta)\left(\dot{\theta}+\frac{a_1}{a_2}\dot{\phi}\right)\right)\right] dV, \tag{A.5}$$

$$\dot{\mathcal{H}}_{21} = \frac{d}{dt}\int_V \rho\left[\xi_1^2\sin(\theta)\left(\frac{\dot{a}_1}{a_1}\cos(\theta)-\sin(\theta)\left(\dot{\theta}+\frac{a_2}{a_1}\dot{\phi}\right)\right) + \xi_2^2\cos(\theta)\left(-\frac{\dot{a}_2}{a_2}\sin(\theta)-\cos(\theta)\left(\dot{\theta}+\frac{a_1}{a_2}\dot{\phi}\right)\right)\right] dV. \tag{A.6}$$

where the terms under the integral sign with $\xi_i\xi_j, i \neq j$ have been suppressed as they will integrate to zero.

Moving ρ outside the integral, integrating, and simplifying yields:

$$\dot{\mathcal{H}}_{11} = \frac{d}{dt}\frac{m}{5}\left[\dot{a}_1 a_1\cos^2(\theta)+\dot{a}_2 a_2\sin^2(\theta) - \frac{1}{2}a_1^2\sin(2\theta)\left(\dot{\theta}+\frac{a_2}{a_1}\dot{\phi}\right)+\frac{1}{2}\sin(2\theta)\left(\dot{\theta}+\frac{a_1}{a_2}\dot{\phi}\right)\right] \tag{A.7}$$

$$\dot{\mathcal{H}}_{22} = \frac{d}{dt}\frac{m}{5}\left[\dot{a}_1 a_1\sin^2(\theta)+\dot{a}_2 a_2\cos^2(\theta) + \frac{1}{2}a_1^2\sin(2\theta)\left(\dot{\theta}+\frac{a_2}{a_1}\dot{\phi}\right)-\frac{1}{2}\sin(2\theta)\left(\dot{\theta}+\frac{a_1}{a_2}\dot{\phi}\right)\right] \tag{A.8}$$

$$\dot{\mathcal{H}}_{33} = \frac{d}{dt}\frac{m}{5}\left[\dot{a}_3 a_3\right] \tag{A.9}$$

$$\dot{\mathcal{H}}_{12} = \frac{d}{dt}\frac{m}{5}\left[\frac{1}{2}(\dot{a}_1 a_1-\dot{a}_2 a_2)\sin(2\theta)+\dot{\theta}\left(a_1^2\cos^2(\theta)+a_2^2\sin^2(\theta)\right)+a_1 a_2\dot{\phi}\right] \tag{A.10}$$

$$\dot{\mathcal{H}}_{21} = \frac{d}{dt}\frac{m}{5}\left[\frac{1}{2}(\dot{a}_1 a_1-\dot{a}_2 a_2)\sin(2\theta)-\dot{\theta}\left(a_1^2\sin^2(\theta)+a_2^2\cos^2(\theta)\right)-a_1 a_2\dot{\phi}\right] \tag{A.11}$$

Taking the temporal derivative yields Equations 2.34 – 2.37.

B

Numerical integrator error comparison

A comparison of the computational time relative to error thresholds of the SunDials CVODE numerical integrator [used in this work] compared to other available numerical integrators is provided by the authors of the ODES package at https://scikits-odes.readthedocs.io/en/latest/solvers.html#performance-of-the-solvers, where it is shown SunDials is the fastest solver at all error tolerances.

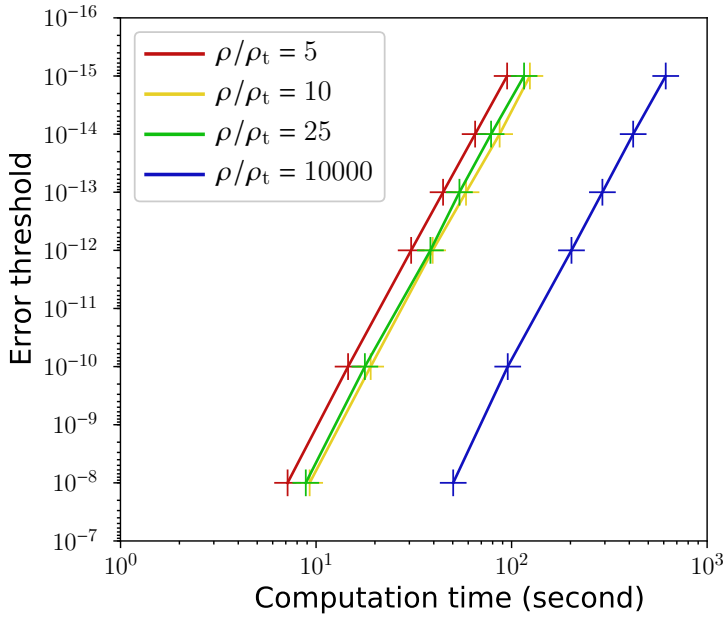

Figure B.1: Computation time of simulations for varying specified error thresholds for several cases with differing tidal strengths. The simulation times are represented by + symbols with the curve being extrapolated from the data points. A value of 10^{-16} represents approximately numerical precision.

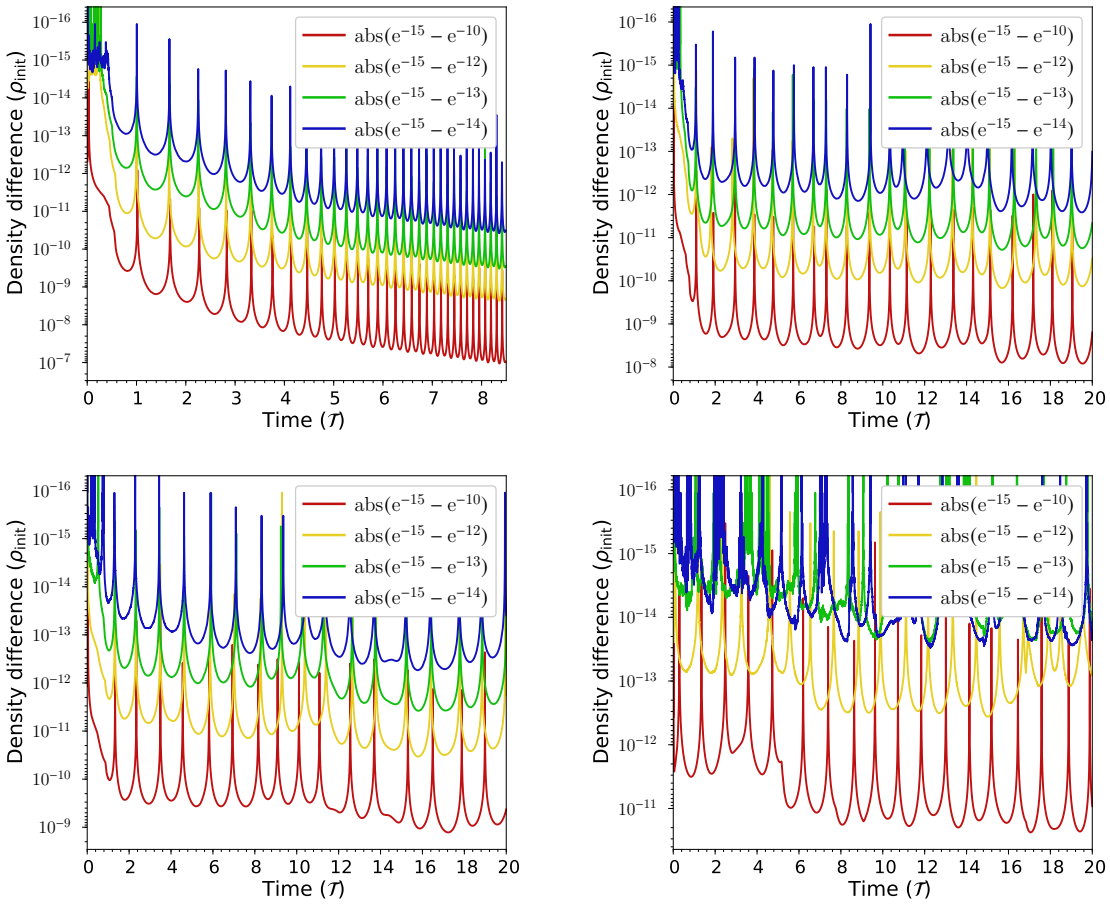

Figure B.2: Comparison of density values for varying error tolerances for tidal strengths of (clockwise from top right) $\rho/\rho_{\text{t}} = 5,\ 10,\ 25,\ 10000$. In the legend e^{-x} represents a specified relative *and* absolute error threshold of 10^{-x}. The value of 10^{-15} represents the smallest calculable error, choosing a smaller value is in the regime of numerical precision. Typical density values are of order unity and hence choosing a error of 10^{-12} yields no significant error in calculations.

C

List of software applications and packages

This thesis used the following web applications:

NASA's Astrophysics Data System Bibliographic Services - A Digital Library portal for researchers in Astronomy and Physics. https://ui.adsabs.harvard.edu.

This results of this thesis were calculated using the Python programming language (Python Software Foundation, https://www.python.org) with the addition of the following software packages:

attrs[73] - Classes without boilerplate.

Cython[74] - An optimising static compiler for both the Python programming language and the extended Cython programming language

Matplotlib[75] - A Python 2D plotting library.

Mpmath[76] - A Python library for real and complex floating-point arithmetic.

NumPy[77,78] - A scientific computing package.

ODES[68] - A high level interface to ODE and DAE solvers, provided through scikits.

Scipy[79,80] - A Python-based ecosystem of open-source software for mathematics, science, and engineering.

SunDials[67] - A suite of nonlinear and differential/algebraic equation solvers.

References

[1] M. Morris. *Massive star formation near the Galactic center and the fate of the stellar remnants*. The Astrophysical Journal **408**, 496 (1993).

[2] W. J. Forrest, M. A. Shure, J. L. Pipher, and C. E. Woodward. *Brackett alpha images of the Galactic center*. AIP Conference Proceedings **155**(1), 153 (1987).

[3] D. Allen, A. Hyland, and D. Hillier. *The source of luminosity at the Galactic Centre*. Monthly Notices of the Royal Astronomical Society **244**, 706 (1990).

[4] J. R. Lu, A. M. Ghez, S. D. Hornstein, M. R. Morris, E. E. Becklin, and K. Matthews. *A disk of young stars at the galactic center as determined by individual stellar orbits*. The Astrophysical Journal **690**(2), 1463 (2008).

[5] J. R. Lu, A. M. Ghez, M. R. Morris, W. Clarkson, A. Stolte, T. Do, S. Yelda, and J. Anderson. *Young stars in the Galactic center*. Proceedings of the International Astronomical Union **9**(S303), 211 (2013).

[6] S. Gillessen, F. Eisenhauer, S. Trippe, T. Alexander, R. Genzel, F. Martins, and T. Ott. *Monitoring stellar orbits around the massive black hole in the galactic center*. The Astrophysical Journal **692**(2), 1075 (2009).

[7] M. Wardle and F. Yusef-Zadeh. *On the Formation of Compact Stellar Disks around Sagittarius A**. The Astrophysical Journal **683**(1), L37 (2008).

[8] M. Mapelli, T. Hayfield, L. Mayer, and J. Wadsley. *In situ formation of Sgr A* stars via disk fragmentation: parent cloud properties and thermodynamics*. The Astrophysical Journal **749**(2), 168 (2012).

[9] A. Eckart, J. Moultaka, T. Viehmann, C. Straubmeier, and N. Mouawad. *Young Stars at the Center of the Milky Way?* The Astrophysical Journal **602**(2), 760 (2004).

[10] K. Mužić, R. Schödel, A. Eckart, L. Meyer, and A. Zensus. *IRS 13n: a new comoving group of sources at the Galactic center*. Astronomy & Astrophysics **482**(1), 173 (2008).

[11] A. Eckart, K. Mužić, S. Yazici, N. Sabha, B. Shahzamanian, G. Witzel, L. Moser, M. Garcia-Marin, M. Valencia-S, B. Jalali, M. Bremer, C. Straubmeier, C. Rauch, R. Buchholz, D. Kunneriath, and J. Moultaka. *Near-infrared proper motions and spectroscopy of infrared excess sources at the Galactic center*. Astronomy & Astrophysics **551**, A18 (2013).

[12] T. Yoshikawa, S. Nishiyama, M. Tamura, M. Ishii, and T. Nagata. *Intrinsically polarized stars and implication for star formation in the central parsec of our galaxy*. The Astrophysical Journal **778**(2), 92 (2013).

[13] F. Yusef-Zadeh, M. Royster, M. Wardle, R. Arendt, H. Bushouse, D. C. Lis, M. W. Pound, D. A. Roberts, B. Whitney, and A. Wootten. *ALMA observations of the galactic center: SiO outflows and high-mass star formation near Sgr A**. The Astrophysical Journal Letters **767**(2), L32 (2013).

[14] F. Yusef-Zadeh, D. A. Roberts, M. Wardle, W. Cotton, R. Schödel, and M. J. Royster. *Radio continuum observations of the galactic center: Photoevaporative proplyd-like objects near Sgr A**. The Astrophysical Journal **801**(2), L26 (2015).

[15] F. Yusef-Zadeh, M. Wardle, D. Kunneriath, M. Royster, A. Wootten, and D. A. Roberts. *ALMA Detection of Bipolar Outflows: Evidence for Low Mass Star Formation within 1pc of Sgr A**. The Astrophysical Journal Letters **850**(2), L30 (2017).

[16] M. J. Reid. *The Distance to the Center of the Galaxy*. Annual Review of Astronomy and Astrophysics **31**(1), 345 (1993).

[17] F. Eisenhauer, R. Genzel, T. Alexander, R. Abuter, T. Paumard, T. Ott, A. Gilbert, S. Gillessen, M. Horrobin, S. Trippe, H. Bonnet, C. Dumas, N. Hubin, A. Kaufer, M. Kissler-Patig, G. Monnet, S. Strobele, T. Szeifert, A. Eckart, R. Schodel, and S. Zucker. *Sinfoni in the Galactic Center: Young Stars and Infrared Flares in the Central Light-Month*. The Astrophysical Journal **628**(1), 246 (2005).

[18] A. M. Ghez, S. Salim, N. N. Weinberg, J. R. Lu, T. Do, J. K. Dunn, K. Matthews, M. R. Morris, S. Yelda, E. E. Becklin, T. Kremenek, M. Milosavljevic, and J. Naiman. *Measuring Distance and Properties of the Milky Way's Central Supermassive Black Hole with Stellar Orbits*. The Astrophysical Journal **689**(2), 1044 (2008).

[19] S. Gillessen, P. M. Plewa, F. Eisenhauer, R. Sari, I. Waisberg, M. Habibi, O. Pfuhl, E. George, J. Dexter, S. von Fellenberg, T. Ott, and R. Genzel. *An Update on Monitoring Stellar Orbits in the Galactic Center*. The Astrophysical Journal **837**(1), 30 (2017).

[20] The GRAVITY Collaboration, R. Abuter, A. Amorim, M. Bauböck, J. P. Berger, H. Bonnet, W. Brandner, Y. Clénet, V. Coudé du Foresto, P. T. de Zeeuw, J. Dexter, G. Duvert, A. Eckart, F. Eisenhauer, N. M. Förster Schreiber, P. Garcia, F. Gao, E. Gendron, R. Genzel, O. Gerhard, S. Gillessen, M. Habibi, X. Haubois, T. Henning, S. Hippler, M. Horrobin, A. Jiménez-Rosales, L. Jocou, P. Kervella, S. Lacour, V. Lapeyrère, J.-B. Le Bouquin, P. Léna, T. Ott, T. Paumard, K. Perraut, G. Perrin, O. Pfuhl, S. Rabien, G. Rodriguez Coira, G. Rousset, S. Scheithauer, A. Sternberg, O. Straub, C. Straubmeier, E. Sturm, L. J. Tacconi, F. Vincent, S. von Fellenberg, I. Waisberg, F. Widmann, E. Wieprecht, E. Wiezorrek, J. Woillez, and S. Yazici. *A geometric distance measurement to the Galactic center black hole with 0.3% uncertainty*. Astronomy & Astrophysics **625**, L10 (2019).

[21] R. Schödel, T. Ott, R. Genzel, R. Hofmann, M. Lehnert, A. Eckart, N. Mouawad, T. Alexander, M. J. Reid, R. Lenzen, M. Hartung, F. Lacombe, D. Rouan, E. Gendron, G. Rousset, A.-M. Lagrange, W. Brandner, N. Ageorges, C. Lidman, A. F. M. Moorwood, J. Spyromilio, N. Hubin, and K. M. Menten. *A star in a 15.2-year orbit around*

the supermassive black hole at the centre of the Milky Way. Nature **419**(6908), 694 (2002).

[22] E. E. Becklin, I. Gatley, and M. W. Werner. *Far-infrared observations of Sagittarius A - The luminosity and dust density in the central parsec of the Galaxy*. The Astrophysical Journal **258**, 135 (1982).

[23] K. Ferrière. *Interstellar gas within ~10pc of Sagittarius A*. Astronomy & Astrophysics **540**, A50 (2012).

[24] R. Genzel, F. Eisenhauer, and S. Gillessen. *The Galactic Center massive black hole and nuclear star cluster*. Rev. Mod. Phys. **82**(4), 3121 (2010).

[25] K. Y. Lo and M. J. Claussen. *High-resolution observations of ionized gas in central 3 parsecs of the Galaxy: possible evidence for infall*. Nature **306**(5944), 647 (1983).

[26] J. M. Jackson, N. Geis, R. Genzel, A. I. Harris, S. Madden, A. Poglitsch, G. J. Stacey, and C. H. Townes. *Neutral gas in the central 2 parsecs of the Galaxy*. The Astrophysical Journal **402**, 173 (1993).

[27] R. Guesten, R. Genzel, M. Wright, D. Jaffe, J. Stutzki, and A. Harris. *Aperture Synthesis Observations of the Circumnuclear Ring in the Galactic Center*. Astrophysics Journal **318**, 124 (1987).

[28] J.-H. Zhao, R. Blundell, J. M. Moran, D. Downes, K. F. Schuster, and D. P. Marrone. *The high density ionized gas in the central parsec of the galaxy*. The Astrophysical Journal **723**(2), 1097 (2010).

[29] T. Paumard, J.-P. Maillard, and M. Morris. *Kinematic and structural analysis of the Minispiral in the Galactic Center from BEAR spectro-imagery*. Astronomy & Astrophysics **426**(1), 81 (2004).

[30] J. Davidson, M. Werner, X. Wu, D. Lester, P. Harvey, M. Joy, and M. Morris. *The luminosity of the Galactic center*. The Astrophysical Journal **387**, 189 (1992).

[31] R. M. Herrnstein and P. T. P. Ho. *Hot Molecular Gas in the Galactic Center*. The Astrophysical Journal **579**(2), L83 (2002).

[32] F. Yusef-Zadeh, J. Braatz, M. Wardle, and D. Roberts. *Massive Star Formation in the Molecular Ring Orbiting the Black Hole at the Galactic Center*. The Astrophysical Journal Letters **683**(2), L147 (2008).

[33] M. C. H. Wright, A. L. Coil, R. S. McGary, P. T. P. Ho, and A. I. Harris. *Molecular Tracers of the Central 12 Parsecs of the Galactic Center*. The Astrophysical Journal **551**(1), 254 (2001).

[34] R. Genzel, D. M. Watson, M. K. Crawford, and C. H. Townes. *The neutral-gas disk around the galactic center*. The Astrophysical Journal **297**, 766 (1985).

[35] T. Oka, M. Nagai, K. Kamegai, and K. Tanaka. *A new look at the galactic circumnuclear disk*. The Astrophysical Journal p. 10 (2011).

[36] I. L. Smith and M. Wardle. *An analysis of HCN observations of the Circumnuclear Disc at the Galactic Centre*. Monthly Notices of the Royal Astronomical Society **437**(4), 3159 (2014).

[37] M. A. Requena-Torres, R. Güsten, A. Weiß, A. I. Harris, J. Martín-Pintado, J. Stutzki, B. Klein, S. Heyminck, and C. Risacher. *GREAT confirms transient nature of the circum-nuclear disk*. A&A **542**(L21), 4 (2012).

[38] E. A. C. Mills. *The excitation of HCN and HCO+ in the galactic center circumnuclear disk*. The Astrophysical Journal p. 20 (2013).

[39] F. Yusef-Zadeh. *Signatures of young star formation activity with two parsecs of Sgr A**. The Astrophysical Journal p. 18 (2015).

[40] E. Becklin and G. Neugebauer. *Infrared Observations of the Galactic Center*. The Astrophysical Journal **151**, 145 (1968).

[41] E. Becklin and G. Neugebauer. *High-resolution maps of the galactic center at 2.2 and 10 microns*. The Astrophysical Journal Letters **200**, L71 (1975).

[42] E. Becklin, K. Matthews, G. Neugebauer, and S. Willner. *Infrared observations of the galactic center. I - Nature of the compact sources*. The Astrophysical Journal **219**, 121 (1978).

[43] R. Schödel, D. Merritt, and A. Eckart. *The nuclear star cluster of the Milky Way: proper motions and mass* ***. Astronomy & Astrophysics **502**(1), 91 (2009).

[44] A. M. Ghez, S. Salim, S. D. Hornstein, A. Tanner, J. R. Lu, M. Morris, E. E. Becklin, and G. Duchene. *Stellar Orbits around the Galactic Center Black Hole*. The Astrophysical Journal **620**(2), 744 (2005).

[45] T. Paumard, R. Genzel, F. Martins, S. Nayakshin, A. M. Beloborodov, Y. Levin, S. Trippe, F. Eisenhauer, T. Ott, S. Gillessen, R. Abuter, J. Cuadra, T. Alexander, and A. Sternberg. *The two young star disks in the central parsec of the Galaxy: properties, dynamics, and formation*. Journal of Physics: Conference Series **54**, 199 (2006).

[46] Y. Levin and A. M. Beloborodov. *Stellar Disk in the Galactic Center: A Remnant of a Dense Accretion Disk?* The Astrophysical Journal **590**(1), L33 (2003).

[47] O. Gerhard. *The Galactic Center He I Stars: Remains of a Dissolved Young Cluster?* The Astrophysical Journal **546**(1), L39 (2001).

[48] J. Cuadra, P. J. Armitage, and R. D. Alexander. *Stellar dynamical evidence against a cold disc origin for stars in the Galactic Centre*. Monthly Notices of the Royal Astronomical Society: Letters **388**(1), L64 (2008).

[49] F. Yusef-Zadeh, D. A. Roberts, H. Bushouse, M. Wardle, W. Cotton, M. Royster, and G. van Moorsel. *The discovery of radio stars within 10" of Sgr A* at 7mm*. The Astrophysical Journal **792**(1), L1 (2014).

[50] R. Bachiller. *Bipolar Molecular Outflows from Young Stars and Protostars*. Annual Review of Astronomy and Astrophysics **34**(1), 111 (1996).

[51] J. Bally. *Protostellar Outflows*. Annual Review of Astronomy and Astrophysics **54**(1), 491 (2016).

[52] N. E. B. Killeen, K. Y. Lo, and R. Crutcher. *Zeeman measurements of the magnetic fields at the Galactic center*. The Astrophysical Journal **385**, 585 (1992).

[53] R. L. Plante, K. Y. Lo, and R. M. Crutcher. *The magnetic fields in the galactic center: Detection of H1 Zeeman splitting*. The Astrophysical Journal Letters **445**, L113 (1995).

[54] P.-Y. Hsieh, P. M. Koch, W.-T. Kim, P. T. P. Ho, Y.-W. Tang, and H.-H. Wang. *A Magnetic Field Connecting the Galactic Center Circumnuclear Disk with Streamers and Mini-spiral: Implications from 850 μm Polarization Data*. The Astrophysical Journal **862**(2), 150 (2018).

[55] X. Chen, P. Amaro-Seoane, and J. Cuadra. *Stability of Gas Clouds in Galactic Nuclei: An Extended Virial Theorem*. The Astrophysical Journal **819**, 138 (2016).

[56] R. Ebert. *Über die Verdichtung von H I-Gebieten. Mit 5 Textabbildungen*. Zeitschrift für Astrophysik **37**, 217 (1955).

[57] W. Bonnor. *Boyle's Law and Gravitational Instability*. Monthly Notices of the Royal Astronomical Society **116**(3), 351 (1956).

[58] S. Chandrasekhar. *Ellipsoidal figures of equilibrium* (Yale Univeristy Press, 1969). Publication Title: The Silliman Foundation Lectures, New Haven: Yale University Press, 1969.

[59] L. Landau and E. Lifshitz. *Fluid Mechanics* (Butterworth-Heinemann, 1987), 2 ed.

[60] J. W. S. Rayleigh. *Scientific Papers*, vol. 4 (Cambridge University Press, Cambridge, 1903).

[61] S. Chandrasekhar and E. Fermi. *Problems of Gravitational Stability in the Presence of a Magnetic Field.* The Astrophysical Journal **118**, 116 (1953).

[62] E. N. Parker. *The Gross Dynamics of a Hydromagnetic Gas Cloud.* The Astrophysical Journal Supplement Series **3**, 51 (1957).

[63] W. H. McCrea. *The formation of Population I Stars. Part I. Gravitational contraction*. Monthly Notices of the Royal Astronomical Society **117**, 562 (1957).

[64] N. Lebovitz. *The Virial Tensor and its Application to Self-Gravitating Fluids.* The Astrophysical Journal **134**, 500 (1961).

[65] S. Chandrasekhar and N. Lebovitz. *The Potentials and the Superpotentials of Homogeneous Ellipsoids.* The Astrophysical Journal **136**, 1037 (1962).

[66] S. Chandrasekhar. *The Equilibrium and the Stability of the Roche Ellipsoids.* The Astrophysical Journal **138**, 1182 (1963).

[67] A. C. Hindmarsh, P. N. Brown, K. E. Grant, S. L. Lee, R. Serban, D. E. Shumaker, and C. S. Woodward. *SUNDIALS: Suite of nonlinear and differential/algebraic equation solvers*. ACM Transactions on Mathematical Software (TOMS) **31**(3), 363 (2005).

[68] B. Malengier, P. Kišon, J. Tocknell, C. Abert, F. Bruckner, and M.-A. Bisotti. *ODES: a high level interface to ODE and DAE solvers*. The Journal of Open Source Software **3**(22), 165 (2018).

[69] B. Draine. *Physics of the Interstellar and Intergalactic Medium* (Princeton University Press, Oxfordshire, 2011), 1 ed. Publication Title: Princeton series in Astrophysics.

[70] D. E. Muller. *A Method for Solving Algebraic Equations Using an Automatic Computer*. Mathematical Tables and Other Aids to Computation **10**(56), 208 (1956).

[71] J. J. Moré, B. S. Garbow, and K. E. Hillstrom. *User guide for MINPACK-1*. Tech. Rep. ANL-80-74, Argonne Nat. Lab., Argonne, IL (1980).

[72] C. T. Kelly. *Broyden's Method*. In *Iterative Methods for Linear and Nonlinear Equations*, no. 16 in Frontiers in Applied Mathematics, p. 180 (Society for Industrial and Applied Mathematics, Philadelphia, 1995), 1 ed.

[73] H. Schlawack. *attrs: Classes Without Boilerplate*.

[74] S. Behnel, R. Bradshaw, C. Citro, L. Dalcin, D. S. Seljebotn, and K. Smith. *Cython: The Best of Both Worlds*. Computing in Science Engineering **13**(2), 31 (2011).

[75] J. D. Hunter. *Matplotlib: A 2d Graphics Environment*. Computing in Science Engineering **9**(3), 90 (2007).

[76] F. Johansson and others. *mpmath: a Python library for arbitrary-precision floating-point arithmetic (version 1.1.0)* (2013).

[77] T. E. Oliphant. *A guide to NumPy* (Trelgol Publishing, USA, 2006), 1st ed.

[78] S. van der Walt, S. C. Colbert, and G. Varoquaux. *The NumPy Array: A Structure for Efficient Numerical Computation*. Computing in Science Engineering **13**(2), 22 (2011).

[79] E. Jones, T. Oliphant, P. Peterson, and others. *SciPy: Open source scientific tools for Python*.

[80] R. P. Brent. *Algorithms for Minimization without Derivatives* (Prentice-Hall, Englewood Cliffs, N.J, 1973).